Materials & Design 253 (2025) 113845

Contents lists available at ScienceDirect

Materials & Design

journal homepage: www.elsevier.com/locate/matdes

Correlation between nanomechanical properties and microstructural design concepts of bivalve muscle attachment sites

S. Hoerl [a,*], C. Micheletti [b], S. Amini [b], E. Griesshaber [a], K.-U. Hess [a], A.G. Checa [c,d], M. Peharda [e], W.W. Schmahl [a]

[a] Department of Geo- and Environmental Sciences, Ludwig-Maximilians-Universität München, Munich, Germany
[b] Max Planck Institute of Colloids and Interfaces, Department of Biomaterials, Potsdam, Germany
[c] Instituto Andaluz de Ciencias de la Tierra, CSIC-Universidad de Granada, Armilla, Spain
[d] Departamento de Estratigrafía y Paleontología, Universidad de Granada, Granada, Spain
[e] Institute of Oceanography and Fisheries, Split, Croatia

ARTICLE INFO

Keywords:
Bivalves
Nanoindentation
Microstructure/texture
Myostraca
EBSD

ABSTRACT

Bivalves populate various marine environments and follow diverse lifestyles: attaching to substrates, burrowing into sediments or swimming in water. Their shells play a crucial role in the survival of organisms as they shield the soft tissue from external attacks and facilitate their respective lifestyles. Valve movement is controlled by one or two adductor muscles and the hinge. While the function and structure of adductor muscles can vary, the shell-muscle attachment develops the myostracum, a unique microstructural design. Sectioned parallel and perpendicular to the inner shell surface, we investigated myostracal and non-myostracal microstructures, textures and nanomechanical properties for three bivalve species: The burrowing *Glycymeris pilosa*, the sessile *Chama arcana* and the swimming *Placopecten magellanicus*.

Analyses were conducted using electron backscatter diffraction measurements, laser confocal and backscatter electron imaging, nanoindentation testing and thermogravimetric analysis. We find that the myostracal microstructure is generated mainly through physical determinants, regardless of the bivalve lifestyle and adductor muscle structure. If aragonitic, we show that adjacent shell layers are used as templates for the formation of the myostracal microstructure and highlight how bivalves use the adjacent crystal arrangement to predetermine myostracal microstructure up to inner shell surfaces. Furthermore, this study demonstrates how myostracal layers exceed the hardness of the non-myostracal valves and that of geological aragonite, irrespective of grain size and morphology. Due to the anisotropy of aragonite, we show that aragonite c-axis orientation notably affects the hardness of crystals. The highest hardness is measured when indentation is normal to the shell surface in aragonite c-axes direction.

1. Introduction

Mineralised structures generated under biological control are widely recognised in material science as prototypes for advanced materials. These are organic–inorganic composites and show a large variety of structural design concepts. In particular, molluscs developed a large repertoire of shell-forming microstructural design strategies, which are currently used by material scientists as a valuable source of inspiration for the fabrication of innovative synthetic materials.

Within the molluscan phylum, bivalves are the second most species-rich class after the gastropods [1–3]. Due to their widespread distribution and the lack of major geographical barriers, allopatric isolation is rare in marine environments [4–6]. Because of the high gene flow between populations maintained by their mostly planktonic larvae, bivalves are prime examples of the Marine Speciation Paradox [2,7]. Throughout their highly successful evolutionary history, they have occupied aquatic habitats worldwide, even inhabiting extreme environments such as the polar seas or abyssal marine regions [8–11]. Through diversification mechanisms, bivalves developed a range of motility strategies, such as byssal attachment to substrate, burrowing into sediments or free swimming [12–17].

The most prominent and essential adaptation of bivalves is their hard

---

* Corresponding author.
E-mail address: s.hoerl@lmu.de (S. Hoerl).

https://doi.org/10.1016/j.matdes.2025.113845
Received 25 October 2024; Received in revised form 7 February 2025; Accepted 16 March 2025

exoskeleton, which protects their soft tissue from predators and external chemical and physical hazards. Nonetheless, this is not the only function of the shells. Bivalve shells are also of great importance for adherence to substrate, stability, locomotion and vision [12,18–22]. Bivalve shells are biological composites formed of an organic matrix and a calcium carbonate ($CaCO_3$) polymorph such as aragonite, calcite or (rarely) vaterite [23–25]. The three polymorphs never mix in a microstructure; however, they may comprise different shell layers [24,26–28]. While burrowing and infaunal organisms appear to form predominantly aragonitic shells, bivalves inhabiting other ecological niches are rather bimineralic, with the calcitic layers always being the external shell layers [10,25,29–31].

Valve movement in bivalved organisms is carried out with the adductor and the pedal muscles that attach to the inner surface of the valves. Nonetheless, the opening and closing of the valves are controlled by an interplay between the adductor and pedal muscles and the ligament [32]. At the attachment sites of muscles to the valves, the myostraca, a specific microstructure, develops within the valves. In bivalve shells, myostracal layers are always aragonitic; even in purely calcitic shells, the myostracum consists of aragonite crystals [28,29,33]. It is demonstrated by now that the growth of myostracal crystals is predominantly controlled by a physical process, namely growth competition [28,33–35]. While physical determinants define the microstructure and texture of the myostracum, the organism controls supersaturation, crystal nucleation and the composition of the extracellular polymeric substances. A physical growth process contrasts with the generation of the other shell layers, which are proactively influenced by biological, chemical and stereochemical determinants [36–38]. In layers controlled by non-physical determinants, the biopolymer component is usually organised as a structured matrix; the mineral component fills the structured pattern of voids of the biopolymer matrix [39,40]. Due to their different growth process, myostracal prisms lack an extracellular organic envelope encasing the prisms. Nonetheless, myostraca are also organic-mineral composites. The organic substance is distributed within the prisms; this is an essential requirement for a strong myostracal prism-muscle attachment [41]. The mass fraction of the organic component in most bivalve shells scatters between 0.1–5 wt%, depending on the microstructure of the shell [42–44]. Starting from the periostracum, a primary organic layer that serves as a template for crystal nucleation [45–47], most shell microstructures comprise crystals oriented with their c-axes towards the shell growth surface [28].

The focus of the present study is to discuss the interrelation between biomaterial structure designs and nanomechanical properties. Peter et al. [48] investigated and juxtaposed the latter for a bivalve (*Mytilus galloprovincialis*) and a gastropod (*Haliotis glabra*) shell. This study goes beyond the work of Peter et al. [48], as we discuss here the connection between material structure and its mechanical properties (i) for microstructures formed by distinct (physical, biological) growth determinants, however, being present in the same shell and (ii) for the shells of bivalves that follow distinct lifestyles.

The selected bivalves (*Glycymeris pilosa* (Linnaeus, 1767), *Chama arcana* F. R. Bernard, 1976, and *Placopecten magellanicus* (Gmelin, 1791)) form thick but differently-sized shells, live in different habitats and have distinct lifestyles. *G. pilosa* is found along the coastlines of the Mediterranean Sea and forms large (more than 75 mm diameter in shell length) and thick shells with distinct growth patterns [49,50]. These characteristics, together with the outstanding longevity of some Glycymerididae [51,52], render *Glycymeris* a promising candidate for recording environmental conditions [50,53,54]. *G. pilosa* lacks a functional byssus and secretes solely aragonitic shells adapted for anterior-posterior rocking locomotion during burrowing [55,56]. *C. arcana* is found in warm and intertidal environments of the East Pacific, within the upper 30 m of the water column [57]. Chamidae are sedentary bivalves that cement to a substrate, leading most species to form differently valved shells [58–60]. Adult organisms need large and elongated adductor muscles to ensure the valves' rapid and prolonged closure in turbid environments [61]. While most *Chama* species form purely aragonitic shells, *C. arcana* shells comprise an ornamentation covering consisting of calcite [33,57]. Of the three species investigated in this study, *P. magellanicus* is the most mobile and has developed the ability to swim [62,63]. Organisms go through different stages of mobility. Veligers are pelagic for 30–50 days, and juveniles attach a byssus to rigid substrates [63–66]. As adults, the swimming behaviour of *P. magellanicus* changes with shell size: small scallops (<30 mm) only swim short distances, while large scallops (>100 mm) are mostly sedentary [63,67–70]. Among pectinids, *P. magellanicus* is the fastest swimmer and has the highest hydrodynamic efficiency. Within *P. magellanicus*, adult organisms with medium-sized shells are the most mobile and reach the highest swimming speeds [71]. *P. magellanicus* forms thin shells. As adductor muscle movement is essential for its active locomotion [63,72,73], the adductor muscle and its attachment to the shell are very prominent in *P. magellanicus* shells.

Accordingly, our study has the following objectives:

1. We highlight first the microstructure design concept, mineral phase and texture (crystallographic preferred orientation) of myostracal and non-myostracal valve portions for a bivalve species that burrows into the sediment, a species that lives attached to a substrate and a species that can swim fast and intensely through the water.
2. As the valves are opened and closed via muscles that attach to the myostracal valve portions, we place particular interest in understanding the structural and nanomechanical characteristics of myostraca of the selected species following different lifestyles. We highlight the microstructural designs and textures of the shell layers and the adductor myostraca and discuss how these might relate to the mobility and living behaviour of the organisms.
3. A central objective of this study is to present and discuss the selected bivalves' nanomechanical property results for the valves and the myostraca. We examine whether differences in microstructural designs affect nanomechanical properties, such as indentation elastic modulus and hardness.

Due to the anisotropy of calcite and aragonite crystals [74,75], the crystallographic orientation of crystals can impact nanomechanical property results. Anisotropy is a directional dependence of material properties within crystallographic arrangements [76,77]. This behaviour is well-investigated for ceramics, rocks and metals [78–80]; however, anisotropy and its influence on mechanical response or functional performance of structural biomaterials are generally neglected. Investigating the directional variability of nanomechanical properties for biological hard tissues is essential for comparing material properties between different structural biomaterials and optimising specific man-made materials.

4. Accordingly, we investigate for selected biomineralised hard tissues the orientational variability of nanomechanical properties for bivalve myostracal and non-myostracal valve sections. We compare the nanomechanical response of a biomaterial formed mainly through the control of a physical growth determinant (the myostraca) and a biomaterial formed under biological growth determinants (the non-myostracal shell). We discuss how the anisotropy of aragonite crystals correlates with the measured nanomechanical property results.

Microstructure, texture, and nanomechanical properties were obtained with Electron Backscatter Diffraction (EBSD), field emission scanning electron microscopy (FE-SEM), and depth-sensing nanoindentation. The organic contents of various shell layers were determined using thermogravimetric analysis (TGA). To gain information on the 3D structure and anisotropic behaviour of the shell-forming crystals, measurements were performed in two directions: on perpendicular (Cut 1) and parallel (Cut 2) sections to the inner shell surface (Fig. AP1).

2. Materials and Methods

2.1. Materials

We investigated the shells of the three bivalve species *Glycymeris pilosa* (Linnaeus, 1767), *Chama arcana* (F. R. Bernard, 1976) and *Placopecten magellanicus* (Gmelin, 1791). Specimens were live collected, and care was taken to ensure that all investigated specimens were shells of adult organisms. Specimens of *G. pilosa* were sampled in the Pašman channel, Adriatic Sea. Shells of *C. arcana* were sampled near Newport Beach, CA, USA and obtained from collections of the Natural History Museum (London, UK). Specimens of *P. magellanicus* were collected in deep water off the shore of Nova Scotia, Canada.

2.2. Methods

2.2.1. Sample preparation for electron backscattered diffraction (EBSD) measurements and nanoindentation testing

All shells were sectioned in two directions (Cut 1 and Cut 2), and EBSD and nanoindentation measurements were performed on both cuts. Appendix Figure AP1 indicates the cuts through the shells. **Cut 1** is perpendicular to the inner shell surface; EBSD and nanoindentation measurements were performed on a cross-section, distal to proximal, through the shell. Accordingly, the nanoindents were placed parallel to the inner shell surface. **Cut 2** is parallel to the inner shell surface; EBSD and nanoindentation measurements were performed perpendicular to the inner shell surface. Accordingly, the nanoindents were placed perpendicular to the inner shell surface.

For all investigated species, sample surfaces were prepared perpendicular and parallel to the growth direction (Appendix Figure AP1a, b). Analysing samples along two cuts gives a representative and three-dimensional overview of the adductor myostraca and adjacent shell layers since EBSD and nanoindentation testing mostly give information about the properties of the exposed sample surface. The valves were cut through the adductor myostraca (Appendix Figure AP1c-f). The obtained shell pieces were embedded into epoxy resin and were subjected to several mechanical grinding and polishing steps. The final polishing step consisted of etch-polishing with colloidal alumina (particle size ~ 0.06 μm) in a vibratory polisher. For Cut 1, the shell pieces were polished perpendicular to the inner myostracal surface, exposing a transversal cross-section from the inner to the outer shell surface. For Cut 2, the shell pieces were polished parallel to the myostracal layers, exposing only the inner shell surface.

For EBSD measurements, samples were coated with 4–6 nm carbon for FE-SEM imaging with 5 nm Pt/Pd. For laser confocal microscopy imaging and nanoindentation testing, sample surfaces were not coated.

2.2.2. Secondary electron (SE), backscatter electron (BSE) imaging and electron backscattered diffraction (EBSD) measurements

SE, BSE imaging and EBSD measurements were carried out with a Hitachi SU5000 field emission SEM equipped with an Oxford Instruments Nordlys Nano EBSD detector. EBSD scans were taken at 20 kV and were performed with a step size of 200 to 450 nm. For indexing the aragonite EBSD patterns, the unit cell setting: $a_0 = 4.9614(3)$ Å, $b_0 = 7.9671(4)$ Å, $c_0 = 5.7404(4)$ Å was used. EBSD data were evaluated with the Oxford Instruments AZTEC Crystal and CHANNEL 5 HKL software.

2.2.3. Nanoindentation testing

Nanoindentation measurements were conducted using a Hysitron Triboindenter TI-950 nanomechanical tester (Bruker, USA) equipped with a 2D standard transducer and a diamond Berkovich tip. A load function of 5 s-2 s-5 s (loading-holding-unloading) with a peak force of 1 mN and a holding time of 2 s at maximum load was applied at each measurement. Tip areas were calibrated using standard fused quartz and aluminium samples for the required contact depths. The indentation elastic modulus and the hardness values were determined via the unloading curve according to the Oliver-Pharr method in the Hysitron software [81,82]. Indents with curves displaying anomalous behaviour or artefacts (e.g., due to the sample or tip moving during indentation) were discarded from indentation elastic modulus and hardness calculations. The indented aragonite and calcite references are from non-biogenic single crystals. Both non-biological references were indented with c-axes misoriented 35-40° to the indentation direction. This c-axis orientation is close to {104}, an orientation that was recently tested to yield average values for hardness and elastic modulus in geological calcite [83]. For every measured microstructure, we performed maps and/or profiles consisting of at least 60 nanoindents. The instrument was calibrated before each use to guarantee correlation between tip position and optical image.

2.2.4. Thermogravimetric analysis (TGA)

Samples of crossed-lamellar, complex crossed-lamellar and myostracal aragonite, as well as foliated calcite, were drilled utilising a high-precision dental drill from the respective shell portions. Up to 40 mg of powder were obtained for analysis. TGA measurements were performed with a Netzsch STA 449 F1. The samples were heated from room temperature to 600 °C at a constant rate of 10 °C per minute in a static-air atmosphere. Approximately 20 mg of each sample was used for TGA analysis in an open aluminium oxide crucible. Each sample was measured twice, except for one. The error margin for individual measurements is ± 0.05 wt%; however, crossed-lamellar and myostracal layers of *G. pilosa* showed small heterogeneities.

No prior drying of the samples was performed. The weight loss between 25 °C and 100 °C is attributed to adsorbed water. Separate measurements on pure inorganic carbonate samples (calcite and aragonite) under the same conditions showed decarbonisation beginning around 500 °C, with a weight loss of 0.03 wt% at 540 °C for both samples. Therefore, the study reports mass loss between 100 °C and 540 °C, as detailed in Figure AP4.

2.2.5. Terminology

Subsequently, we define the structural and nanomechanical property terms used in this study. For further information concerning nanoindentation testing, see [74,75]; for EBSD, see [84]; for crystal twin formation, see [85–87].

Microstructure refers to the sizes, morphologies, co– and misorientations, and modes of interlinkage of crystal grains in a material. It is shown with colour-coded EBSD maps, where similar colours reflect similar crystal orientations, and different colours highlight differences in crystal orientation. The acquisition coordinate system is indicated in the a-axes pole figures in Fig. 1a, b and is consistent for all EBSD scans presented in this contribution.

Pole figures are stereographic projections of crystallographic plane-normal or axes orientations measured for all pixels of an EBSD map or selected areas (subsets). The viewing direction of the pole figures is the same as the viewing direction of the corresponding EBSD maps. All pole figures shown here display the lower hemisphere. Showing data points on the lower hemisphere of the stereographic projection ensures that the pole figures are displayed in the same spatial orientation as the corresponding EBSD map. With pole figures, we either show individual orientation data points or the density distributions of the orientation data.

Texture or *crystallographic preferred orientation* relates to the distribution of all crystal orientations within a material. It is illustrated with pole figures which show either the colour-coded orientation data or the contoured version of the density distribution of the a-, b-, and c-axes poles. In our study, we observe two texture modes: (i) a three-dimensionally ordered, 3D “single-crystal-like” texture and (ii) an axial/cylindrical texture.

A *3D “single-crystal-like” texture* is present when clear-cut maxima are observed in the pole figures of all crystallographic axes. Accordingly, for calcite, we need to observe in the pole figure one cluster for the c-

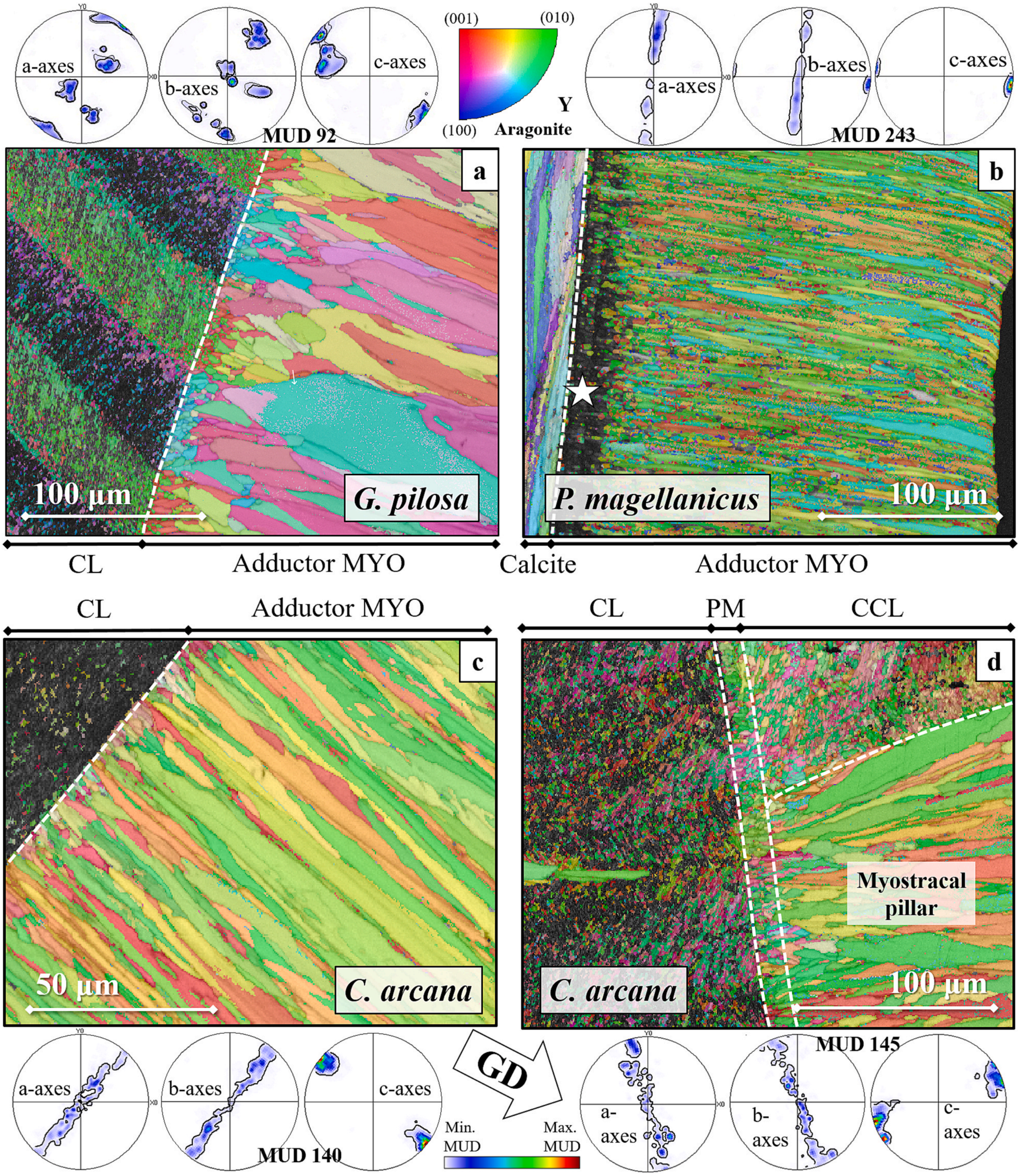

Fig. 1. Microstructure and texture of myostracal regions sectioned and polished perpendicular to the inner shell surface (Cut 1). Colour-coded EBSD maps show the crystal orientation patterns and are complemented by pole figures indicating the orientational probability density distributions of the pure myostraca (a-d). The projection direction and x-y coordinate orientation of the pole figures are equal to the viewing direction and x-y directions (edges) of the corresponding EBSD scan images. The pole figure In *Glycymeris pilosa*, the 3D "single-crystal-like" texture of the crossed-lamellar (CL) layer propagates into the adductor myostracal (MYO) layer (a). The myostracal crystals start as small, isometric grains at the changeover region and become more prismatic and co-oriented as they grow towards the inner shell surface (a). The shell-myostracum interface in *Placopecten magellanicus* is sharp, and an organic-rich layer, visualised by many zero-solution data points, defines the first few µm of the aragonitic layer (white star in b). Towards the inner shell surface, the myostracum comprises long (up to 100 µm), needle-shaped crystals with an axial texture (b). Small, granular crystals initiate the axial adductor myostracum in *Chama arcana* (c) from the changeover with the crossed-lamellar layer. The needle-shaped crystals increase in size and thickness with distance from the changeover. The myostracal pillars in *C. arcana* originate in the pallial myostracum (PM) and have a microstructure similar to the adductor myostracum (d). They have a cone-shaped morphology and grow alongside the complex crossed-lamellar layer (CCL). For all measurements, the approximate growth direction (GD) is indicated by a white arrow.

axes and three clusters for the a-axes; for aragonite one maximum in the pole figure for the a, − b- and c-axes, respectively.

An *axial/cylindrical texture* is developed in the relevant material when the c-axes cluster in one particular direction and the a- and b-axes scatter in orientation on a great circle perpendicular to the c-axis orientation.

A *turbostratic texture* is given when a larger-scale structure is formed of units arranged in a turbulent way with crystallites in the unit strongly structured parallel or subparallel. In foliated calcite layers, we find graded calcite c- and a*-axes with strongly structured, ring-shaped orientation distributions in the pole figures.

Crystal co-orientation statistics are derived from Kikuchi patterns measured at each pixel of an EBSD map. The degree of aragonite/calcite co-orientation within individual crystals is obtained from measurements of the orientational density distribution, the multiple of uniform (random) distribution (MUD) value.

The *MUD value* is calculated by the CHANNEL 5 EBSD software and is an indication of the strength of crystal co-orientation. A high MUD indicates high crystal co-orientation and low MUD values indicate low to random crystallite and/or mineral unit co-orientation. For the parameters fixed for our study (half width of 5 and a cluster size of 3), an MUD value of 700 indicates single-crystallinity, and an MUD value of 1 indicates poly-crystallinity. The given MUD values indicate the crystal co-orientation strength for the described EBSD scan (or a subset of it) and do not apply to the entire volume of a microstructure.

The EBSD *band contrast map* depicts the signal strength of the Kikuchi pattern at each measurement point in the EBSD scan. It is displayed as a grey-scale component in the map; white to light grey colours indicate a high intensity of the Kikuchi signal, corresponding to strong mineralisation, dark grey and black colours point to a weak or absent Kikuchi signal, e.g. when organic matter is scanned.

Grain size statistics are determined via the Oxford Instruments AZtecCrystal software. The bar charts display the area-weighted fractions. For mean value calculations, pseudosymmetries and wild spikes were filtered, and border grains were included.

Twinned crystals are entities in which adjacent crystals of the same phase are intergrown in a regularly recurring orientation relationship. These crystal orientation states are addressed as the twin domains of a twinned crystal. A regular planar interface of two twin domains is called the composition plane and such a twin is called a contact twin. If the interface is not confined to a plane (or planes), the twin is called a penetration twin. Twinning can occur during the initial growth of the crystal, or it might take place after its formation, resulting from stress or phase transformation. The orientation relationship for the characteristic twin in question is called the twin law. If a twinned entity contains three intergrown domains that are related by a twin law consisting of mirror operations on (110) and $(1\bar{1}0)$ for aragonite, then we call it a *cyclic twin*.

In this contribution, the presence of twinned aragonite is proven via the specific misorientation of the domains at the twin boundary. For aragonite, the misorientation at the twin boundary is a 64° rotation around the c-axis [001]. For this misorientation angle, characteristic peaks shown in the misorientation angle distribution diagram indicate the presence and frequency of twinning. The presence of twinned aragonite is also indicated by specific crystal misorientations in the relevant pole figures.

3. Results

This study details the correlation between the structural and nanomechanical property characteristics of *Glycymeris pilosa*, *Chama arcana* and *Placopecten magellanicus* shells. The shell of *G. pilosa* consists solely of aragonite, while *C. arcana* and *P. magellanicus* shells are formed of both aragonite and calcite.

The mode of crystal arrangement varies significantly for the different layers of the investigated species. To better interpret the results gained in this study, the shells were sectioned in two directions. Cut 1 is perpendicular to the inner shell surface, exposing a cross-section through the shell used for EBSD and nanoindentation measurements. When the shell was sectioned according to Cut 1, nanoindents were placed parallel to the inner shell surface. When sectioning according to Cut 2, the section was parallel to the inner shell surface; EBSD and nanoindentation measurements were performed perpendicular to the inner shell surface.

The microstructures and textures.

Fig. 1 and Appendix Figure AP2 show the microstructure and texture of the aragonitic myostraca and the adjacent shell for the investigated bivalve species. Measurements were performed on shell cross-sections (Cut 1). The shell of *G. pilosa* consists of crossed-lamellar aragonite (CL), with the first-order lamellae parallel to each other and the growth direction (GD, indicated in Fig. 1 with a white arrow between the pole figures). The two sets of the first-order lamellae are inclined to each other and consist of small, lath-shaped third-order lamellae. At the changeover to the adductor myostracum, the orientation pattern of the crossed-lamellar shell functions as a nucleation template for the first-formed myostracal crystals (Fig. 1a). As the myostracal crystal growth mechanism is mostly controlled by the physical determinant of growth competition, (e.g., [28,33–35]), the grain size of prismatic crystals increases drastically towards the inner shell surface (Fig. 1a). The texture of the *G. pilosa* myostracum is 3D “single-crystal like”. *P. magellanicus* shells comprise foliated calcite (FC). This type of microstructure and carbonate polymorph is adjacent to *P. magellanicus* adductor myostraca (Fig. 1b). The interface between shell calcite and myostracal aragonite is sharp. The first ∼ 10 μm of the myostracum show a high fraction of organic material, indicated by the large number of zero solution pixels observed in this shell region (Fig. 1b). The *P. magellanicus* myostracum is formed of long (up to 100 μm) and thin (<5 μm) prisms, which are assembled with a strictly axial texture. The shell of *C. arcana* features arrays of calcitic ornamentations at the outermost shell sections. However, the shell between these ornamentations and the adductor myostracum is purely aragonitic. Like the *G. pilosa* myostracum, the *C. arcana* myostracum is also adjacent to crossed-lamellar aragonite towards the outer shell surface. Towards the inner shell surface, *C. arcana* shells consist of complex crossed-lamellar (CCL) aragonite (Fig. 1c, d). Notable features in *C. arcana* shells are the myostracal pillars that extend towards the inner shell surface and intersect the innermost complex crossed-lamellar shell layer (Fig. 1d). Myostracal pillars are conical structures that originate from the pallial myostracum (Fig. 1d) and maintain a myostracal microstructure up to the inner surface of the shell. The prisms of myostracal pillars reach diameters of around 50 μm. The crystals of both adductor myostraca (Fig. 1c) and myostracal pillars (Fig. 1d) are elongated and large (up to 200 μm in length). Their axial texture and specific microstructure are typical for a physically controlled crystal growth process.

Fig. 2 and Appendix Figure AP3 depict the microstructure and texture of adductor myostraca and the non-myostracal shell sectioned parallel to the inner shell surface (Cut 2) for the three investigated bivalve species. Measurements were taken at the innermost shell surface of the shells of adult organisms. Within the adductor myostraca, we found very irregular prism boundaries and, for the investigated species, a distinct difference in grain/prism size. For *G. pilosa*, grain cross-sections have a diameter of up to 50 μm (Fig. 2a, AP3a). Grain cross-sections of *C. arcana* are smaller than those of *G. pilosa* and have diameters up to 10 μm (Fig. 2b, AP3b). With a size of up to 5 to 6 μm in diameter, we found the smallest grain cross-sections in *P. magellanicus* (Fig. 2c, AP3c). The large prisms in *G. pilosa* and, to a smaller extent, in *C. arcana* and *P. magellanicus* are substructured into multiple, slightly misoriented units (cumulative misorientations up to 5°; e.g., white stars in Fig. 2a).

Regarding the texture of myostracal aragonite (see the pole figures in Fig. 2, AP3), we found that (i) *G. pilosa* has a different texture relative to *C. arcana* and *P. magellanicus* and (ii) crystallographic texture is more disordered in *C. arcana* myostraca, relative to the crystals that form

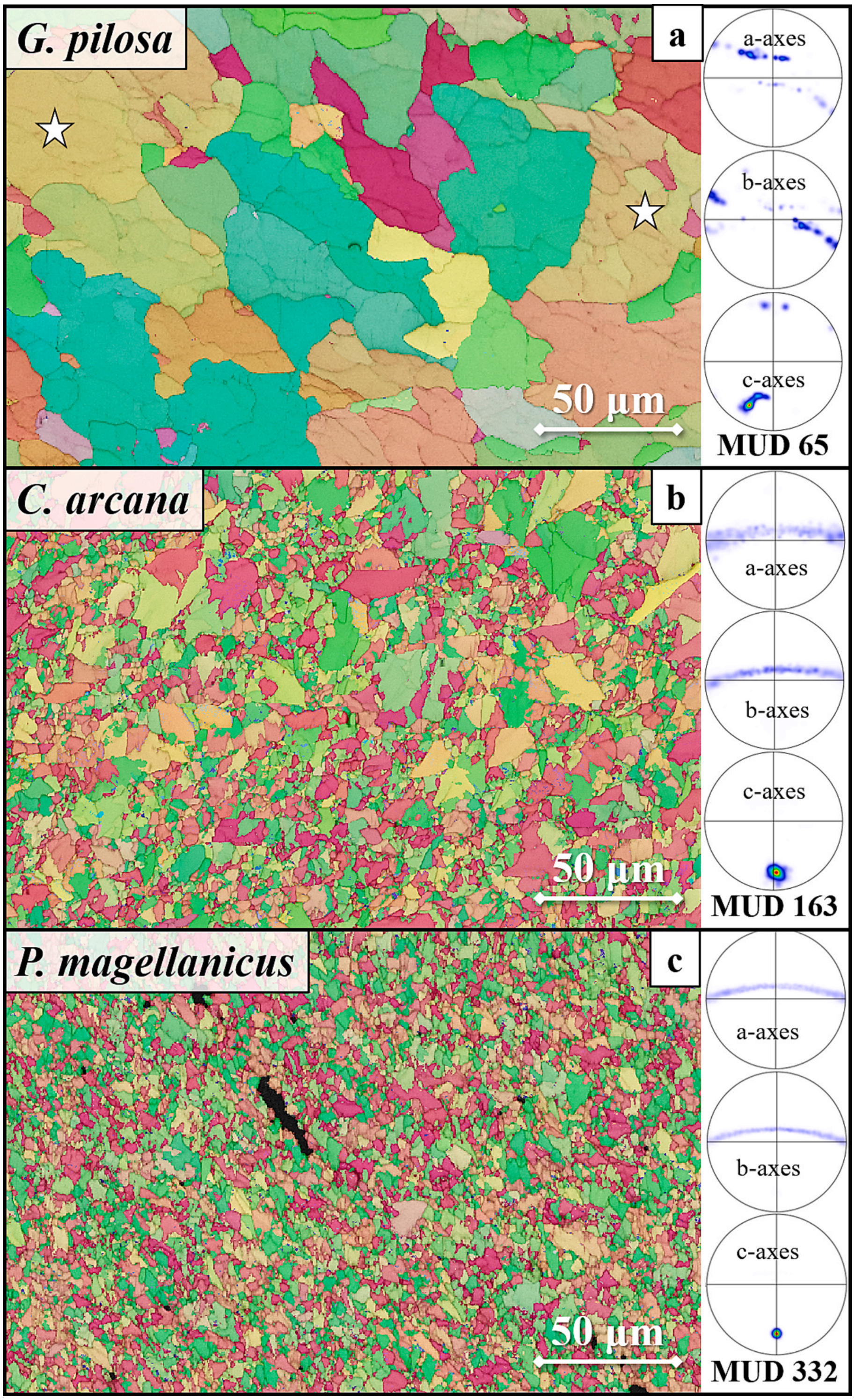

Fig. 2. Microstructure and crystal orientation patterns of adductor myostraca sectioned and polished parallel to the inner shell surface (Cut 2) for the three investigated species. The colour-coded EBSD maps are complemented by pole figures indicating the orientational probability density distributions (a-c). The cross-section of the *G. pilosa* myostracum comprises large (up to 100 µm diameter) irregular prisms that are internally substructured (white stars in a). The 3D "single-crystal-like" texture and the recurring colour-coded crystal orientations indicate that the crossed-lamellar texture of the changeover region (Fig. 1a) is still present at the inner shell surface. In *C. arcana*, the prisms are smaller and neither show a characteristic crystal orientation pattern nor orientation distribution maxima in the axial pole figures (b). *P. magellanicus* shows a texture and microstructure similar to *C. arcana*; however, the grains appear even thinner.

P. magellanicus myostraca (compare the pole figures for *C. arcana* and *P. magellanicus* in Fig. 2, AP3). Therefore, although the *P. magellanicus* myostracum comprises many small prisms (see Fig. 2, AP3), it shows a high degree of crystallographic continuity. The texture of *G. pilosa* adductor myostraca, inherited from the adjacent crossed-lamellar layer, is 3D "single-crystal-like" (well visible from the multiple clustered orientations in the pole figure of Fig. AP3a). In contrast, the texture of *C. arcana* and *P. magellanicus* myostraca is axial (see pole figures in Fig. 2, AP3).

When sectioned parallel to the inner shell surface, the microstructure and crystallographic texture of the shell layers adjacent to the adductor myostracum are well visible (Fig. 3). The contoured pole figures indicate that the crossed-lamellar layer in *G. pilosa* comprises co-oriented first-order lamellae that run mostly parallel to one another (Fig. 3a). On the other hand, *C. arcana* first-order lamellae are strongly interlaced and show a comparatively low co-orientation strength with a weak single-crystal-like to axial texture. The foliated calcite layer of *P. magellanicus* has a turbostratic texture and comprises large (up to 200 μm) sub-structured units (Fig. 3c).

The nanomechanical properties.

Figs. 4, 5 and Table 1 present, for the investigated species, hardness and indentation elastic modulus results for myostracal and non-myostracal valve sections, in addition to nanomechanical property results obtained on non-biological calcite and aragonite references.

For *G. pilosa*, the myostracum is the hardest observed layer, exceeding the hardness of the crossed-lamellar valve and the aragonitic reference (Fig. 4a, b). Depending on the orientation of the myostracal layer towards the loading/unloading direction, the observed nanomechanical properties vary for *G. pilosa*. When indented perpendicular (Cut 2), rather than parallel (Cut 1), to the inner shell surface, the measured hardness of the adductor myostracum is significantly enhanced (Fig. 4a, b). The indentation elastic modulus values of the myostracal layer are comparable for both cuts through the shell; nonetheless, the values obtained perpendicular to the inner shell surface are slightly lower. For *G. pilosa*, The lowest average value for the indentation elastic modulus and hardness was observed for the crossed-lamellar layer.

For *P. magellanicus*, the obtained nanoindentation values show similar results: the calcitic reference has the lowest hardness and indentation elastic modulus of the observed materials (Fig. 4c, d). We found that foliated calcite is significantly harder than geological calcite and also has a slightly increased indentation elastic modulus. For both the parallel and the perpendicular cuts, the myostracum shows the highest hardness (Fig. 4c, d). The average hardness observed perpendicular to the inner shell surface (Cut 2) significantly exceeds the hardness of the myostracum indented parallel to the inner shell layer (Cut 1, Fig. 4c, d). Similar to *G. pilosa*, the obtained mean indentation elastic modulus of the myostracum layer in *P. magellanicus* is slightly decreased when indented perpendicular to the inner shell surface, rather than parallel. For both species, we found that non-biogenic aragonite has a higher indentation elastic modulus than the biological shell layers (Fig. 4a-d).

Along the inner shell surface of *C. arcana*, we found a variety of microstructures: the adductor myostracum, myostracal pillars and the complex crossed-lamellar shell layer. We indented these microstructures perpendicular (Fig. 5a, b) and parallel (Fig. 5c, d) to the inner shell surface. Indentation measurements performed perpendicular to the inner shell surface (Cut 1) show similar results for *C. arcana* to what we measured for the other two bivalve species: the adductor myostracum has the highest observed hardness for all shell layers of *C. arcana* and a high nanoindentation elastic modulus, exceeded only by the modulus of the non-biological reference (Fig. 5a). The hardness of the complex crossed-lamellar aragonite of *C. arcana* exceeds the hardness of the reference and is comparable to the hardness of the myostracal pillars. The observed hardness and elastic modulus for the complex crossed-lamellar layer in *C. arcana* are very similar to the nanoindentation results obtained for the complex crossed-lamellar layer of *Glycymeris* shells, as reported by Hoerl et al. [28]. We found that despite the similarity in microstructure between myostracal pillars and the adductor myostracum, the hardness and indentation elastic modulus of myostracal pillars is lower than that of the adductor myostracum (Fig. 5a, b).

For indentation measurements performed parallel to the inner shell surface (Cut 2) of *C. arcana*, we found similar nanomechanical property relations between the adductor myostracum and the myostracal pillars, both showing enhanced hardness and indentation elastic moduli compared to the aragonite reference. Compared to the myostracal pillars, the adductor myostracum has a significantly higher hardness and indentation elastic modulus (Fig. 5c, d). While the indentation results for the myostracal layers of *C. arcana* followed the trend already observed for *G. pilosa* and *P. magellanicus*, the *C. arcana* complex crossed-lamellar layer differed. When indenting the *C. arcana* complex crossed-lamellar layer perpendicular to the inner shell surface, loading and unloading displacement curves show irregular behaviour (Fig. AP6). The profiles feature many pop-ins, and the anomalously low values for indentation elastic modulus and hardness are related to these. Thus, the measured hardness values are of limited significance for comparisons (Fig. 5d, AP6).

In essence, when comparing the nanoindentation results between Cut 1 and Cut 2, we found for Cut 2 an increase in hardness of about 37 % for *G. pilosa* myostraca, about 20 % for *C. arcana* myostraca and about 15 % for *P. magellanicus* myostraca (Figs. 4, 5, Table 1). The difference in nanoindentation elastic moduli for the different cuts through the shell is less pronounced. For the adductor myostraca of all three investigated species, it is about 3 % (Figs. 4, 5, Table 1). In summary, we found the following trends in nanomechanical properties:

1. For all three investigated species, myostracal aragonite is harder and has a higher indentation elastic modulus relative to the hardness and elastic modulus of the adjacent shell (calcite or aragonite).
2. The complex crossed-lamellar microstructure (CCL) has a higher hardness and a slightly increased indentation elastic modulus relative to the crossed-lamellar (CL) microstructure (for both *C. arcana* and *G. pilosa*).
3. We found a difference in hardness and indentation elastic modulus for measurements performed on the two differently oriented cuts through the shell. The difference is considerable for the hardness; it is present but significantly less notable for indentation elastic modulus results.
4. Of all investigated samples, the hardness and indentation elastic modulus of non-biological calcite is the lowest. The crossed-lamellar (CL) layer shows the lowest hardness and indentation elastic modulus of the investigated aragonitic microstructures. All other aragonitic microstructures surpass the hardness of non-biological aragonite.

4. Discussion

Previous studies describe that the operation of the bivalve adductor muscle depends on the organism's lifestyle and the interaction between the adductor and pedal muscles and the ligament of the hinge [32]. Muscle fibres consist of actin, myosin, and paramyosin [88] and vary in their organisation, type and degree of structural order [88,89]. Depending on the lifestyle and environment of bivalved organisms, adductor muscle fibres may vary in thickness, shape and length [88,90].

Up to three muscle parts relate to bivalve valve opening, closure, and locomotion [91,92]. The *smooth* muscle fibres perform the 'catch' mechanism of the muscle. This slow and continuous contraction helps to achieve tight and energy-efficient valve closure over long periods [91,93,94]. The *obliquely-striated* muscle fibres consist of two overlapping types of muscle filaments that can quickly contract, enabling rapid and strong valve closure. The *cross-striated* muscle fibres in bivalves produce quick contractions. These rapidly squeeze out the water from between the valves and generate a propelling jet of water that can be used for swimming or burrowing [15,95]. Fast and strong valve movements or prolonged valve closure demand that the adductor muscle fibres and myostracal crystals are strongly interlinked. Bivalves achieve tight connections between muscle fibres and shell crystals via a tendon cell layer secreted by the outer mantle epithelium. This tendon cell layer is positioned between the apical ends of the muscle fibres and the basal surface of the myostracal crystals [41,96]. From focal adhesions of the tendon cell layer, myofilament bundles emerge and penetrate the crystals of the myostraca [41]. This leads to one of the strongest

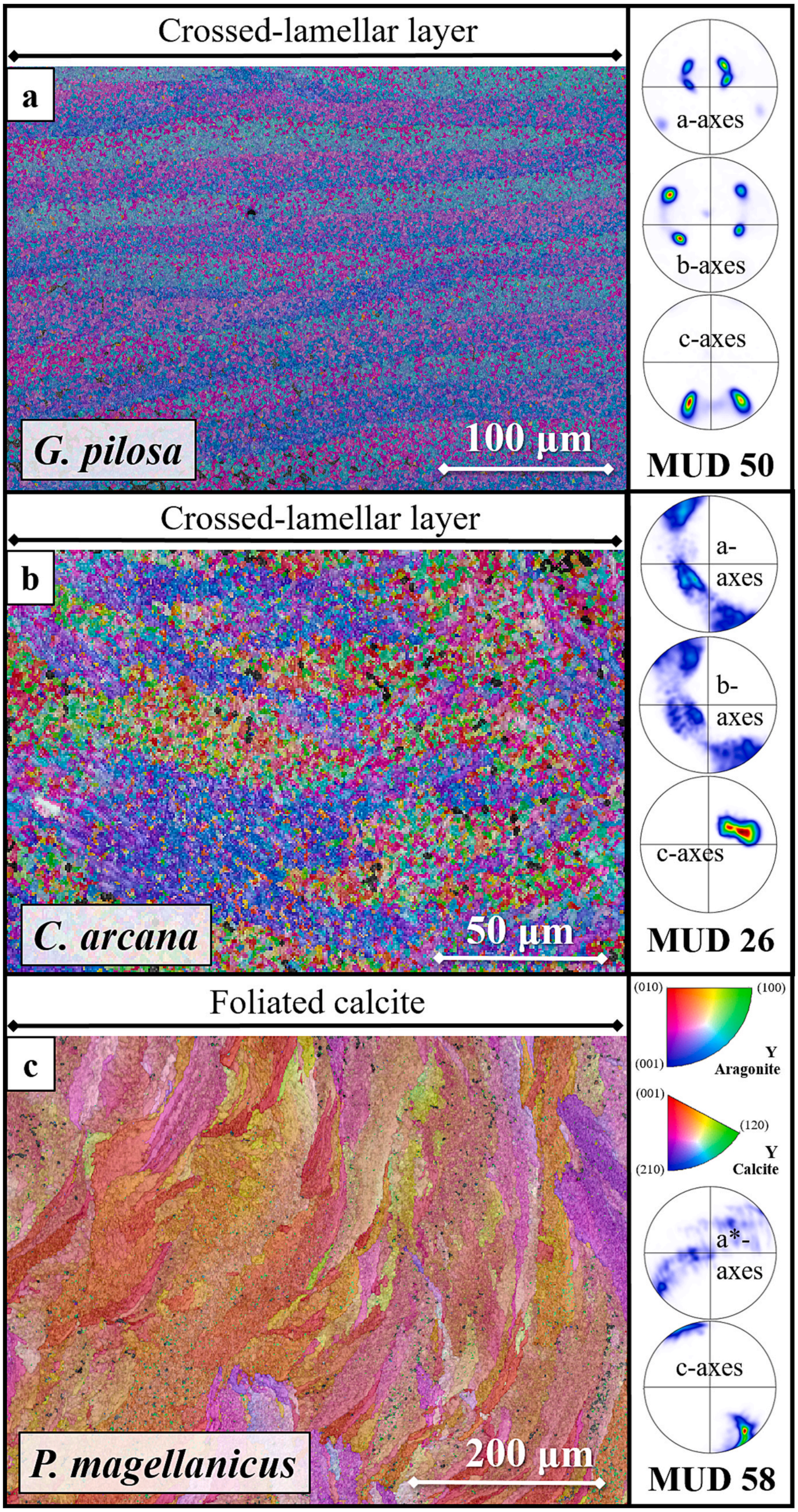

Fig. 3. Microstructure and texture of shell regions adjacent to myostraca sectioned and polished parallel to the inner shell surface (Cut 2). Colour-coded EBSD maps show the microstructure and crystal orientation patterns and are complemented by pole figures indicating the orientational probability density distributions (a-c). In *G. pilosa*, the crossed-lamellar layer has a 3D "single-crystal-like" texture (a), showing two sets of first-order lamellae that run parallel to the growth direction. In *C. arcana*, the crossed-lamellar layer is less co-oriented along the a- and b-axes, and the first-order lamellae do not run straight but are intertwined (b). The foliated calcite layer of *P. magellanicus* comprises large (up to 200 µm) substructured units with an axial texture (c).

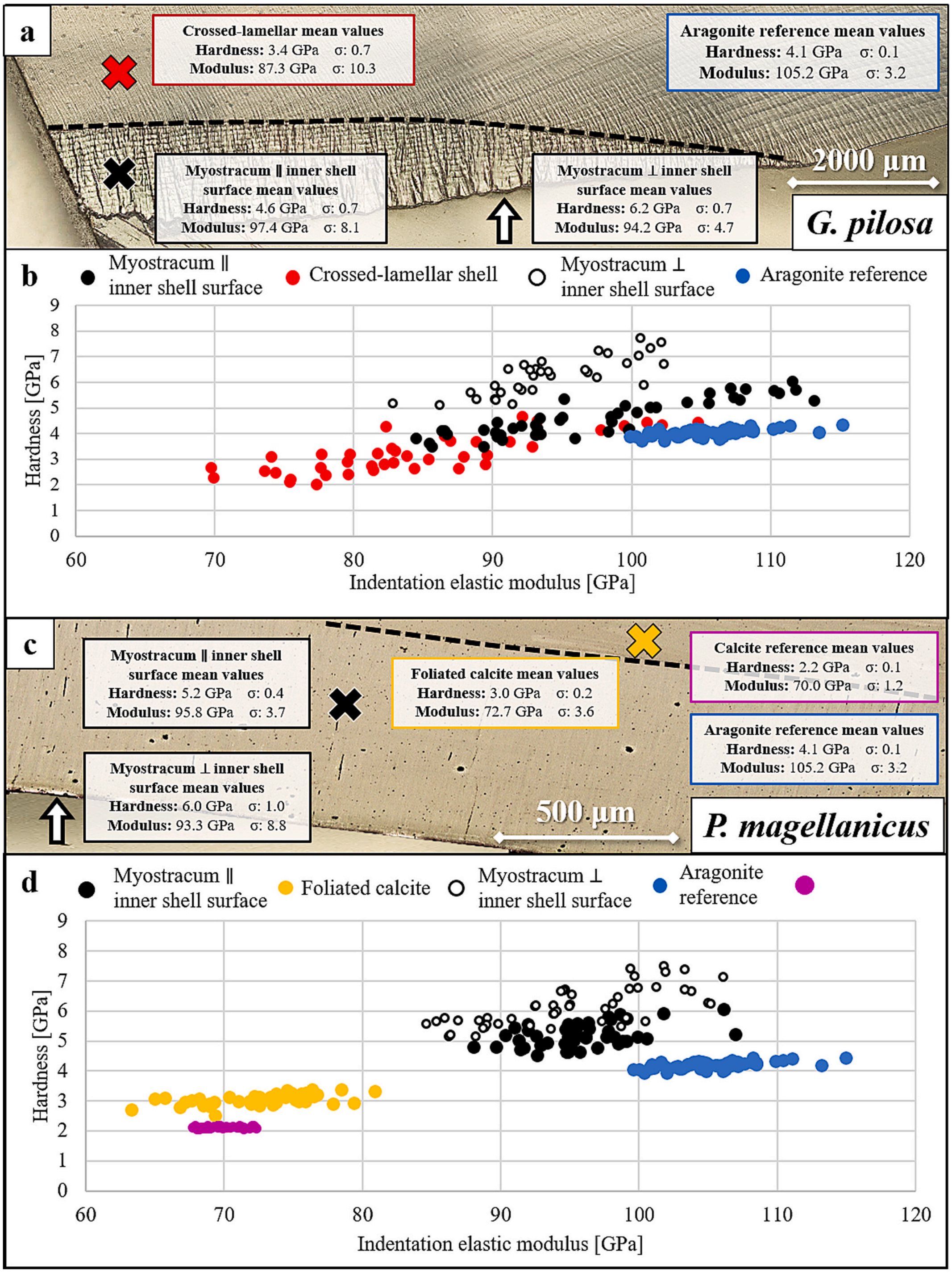

Fig. 4. The hardness and indentation elastic modulus distribution of different layers and cuts of *G. pilosa* and *P. magellanicus* samples with a geological aragonite reference. The confocal laser microscopy images (a, c) depict the different shell layers indented for the two species and give the mean values and standard deviations σ for the hardness and elastic indentation moduli. Measurements were performed in the centre of shell layers (for cut 1, roughly indicated by coloured crosses in a and c) or at the inner shell surface (for cut 2, indicated by coloured arrows in a and c). Plot (b) shows that the myostracum layer (black/white) in *G. pilosa* has a distinctly higher hardness than the crossed-lamellar shell (red) and a non-biological aragonite reference (blue). When indented parallel, rather than perpendicular, to the c-axes orientation, the hardness of the myostracum is increased. This is also visible for *P. magellanicus*, where the myostracum is distinctly harder than the foliated calcite (yellow) or the reference (d). For both species, the indentation elastic modulus of the non-myostracal shell is the lowest. However, the myostracal moduli are lower than geological aragonite. In the geological aragonite reference for both profiles and the geological calcite reference, the crystallographic c-axis is misoriented 35-40°, relative to the indentation direction.

known connection mechanisms utilised by invertebrates or vertebrates [41].

While the muscle structure, function, and fibre interconnection are well-investigated for bivalves by now, only a few studies focused on the role and the structural design of the myostracal hard tissue and the changeover from the non-myostracal shell crystals to the prisms of myostraca. In the subsequent sections, we discuss microstructure, texture and nanomechanical property results of myostraca of sessile,

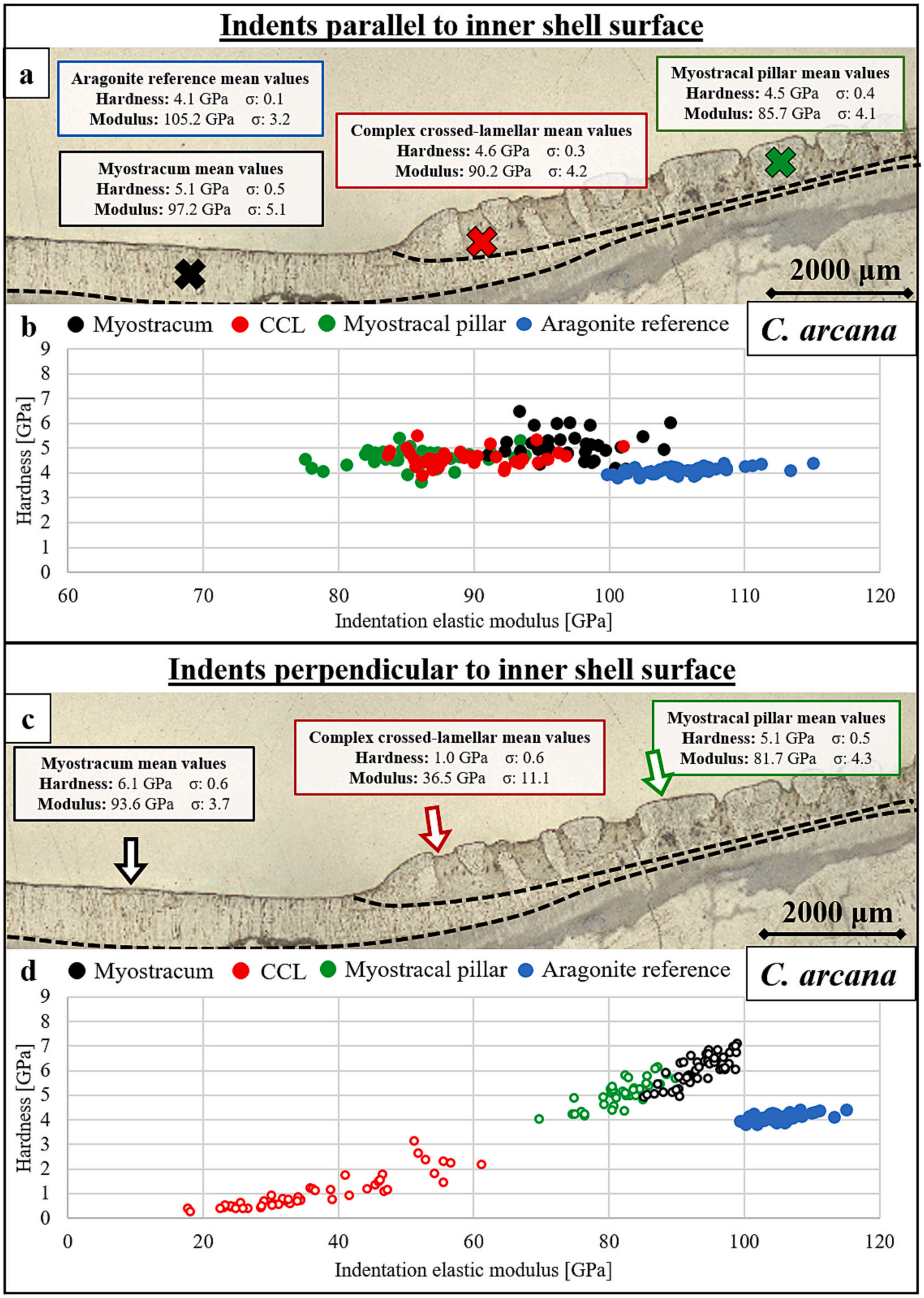

Fig. 5. The hardness and indentation elastic modulus distribution of different layers and indentation directions of *C. arcana* shells with a geological aragonite reference. The confocal laser microscopy images (a, c) display the different indentation directions for the two directions and give the mean values and standard deviations σ for the hardness and elastic indentation moduli. Measurements were performed in the centre of shell layers (for cut 1, roughly indicated by coloured crosses in a) or at the inner shell surface (for cut 2, indicated by coloured arrows in c). Plots (b) and (d) show for different indentation directions that the myostracum layer (black) in *G. pilosa* has a higher hardness than the complex crossed-lamellar shell (red), the myostracal pillars (green) and the geological aragonite reference (blue). When indented parallel, rather than perpendicular, to the c-axes-orientation, the hardness of the myostracum and the myostracal pillars increases (d). For both directions, the highest observed indentation elastic modulus is in the reference, followed by the myostracum and the myostracal pillars. When indented parallel to the c-axes orientations, the complex crossed-lamellar layer showed irregular and distorted displacement curves that might not yield reliable results. In the geological aragonite reference for both profiles, the crystallographic c-axis is misoriented ~ 35° to the indentation direction.

Table 1
Nanoindentation results for maps indented on *G. pilosa*, *C. arcana* and *P. magellanicus* shells. The values are the mean of the indentation measurements reported in this study. The non-biological calcite and aragonite references were tested with c-axes misoriented 35-40° to the indentation direction. Hoerl et al. [28] showed that the complex crossed-lamellar layer in *Glycymeris*, indented parallel to the inner shell surface, is very similar to the complex-crossed-lamellar layer in *Chama*. For the complex crossed-lamellar layer in Glycymerididae, the mean hardness is 4.8 GPa, and the mean indentation elastic modulus is 89.3 GPa [28]. CL: Crossed-lamellar, CCL: Complex crossed-lamellar, FC: Foliated calcite.

	Species	Hardness [GPa]		Indentation elastic modulus [GPa]	
		Indents ‖ to inner shell surface	Indents ⊥ to inner shell surface	Indents ‖ to inner shell surface	Indents ⊥ to inner shell surface
Myostracum	***G. pilosa***	4.6	6.2	97.4	94.4
	C. arcana	5.1	6.1	96.0	93.3
	P. magellanicus	5.2	6.0	97.2	94.0
Shell	***G. pilosa* CL**	3.4		87.3	
	***C. arcana* CL**	3.7		82.2	
	***C. arcana* CCL**	4.6	1.0	90.2	36.5
	P. magellanicus	3.0		72.7	
Geological reference	**Aragonite**	4.1		105.2	
	Calcite	2.2		70.0	

burrowing, and swimming bivalves (Figs. 1 to 6, AP2 to AP6). First, we address the determinants of myostracal microstructures and show that the latter are not only determined by the crystal growth process but also influenced by the microstructure and texture of the adjacent, non-myostracal shell. The shells of the chosen organisms are formed of different microstructures (Fig. 3, AP2); accordingly, different microstructures are adjacent to the myostraca of the investigated bivalve species. Subsequently, we will show that even though the growth process affecting myostracal crystal formation appears to be the same for the different species, the structure of myostraca of bivalves leading different lifestyles is not conservative, as stated by other studies [34,43,97]. The competitively generated myostracal microstructure is modulated by the respective crystal organisation design of the adjacent, non-myostracal shell. Shell crystal organisation is ultimately determined by the shell fabrication requirements imposed on the organism for survival. Second, we discuss the gained nanomechanical property results of myostracal and non-myostracal hard tissue and describe limiting factors for hardness and nanoindentation elastic modulus. Lastly, we discuss for a carbonate biological hard tissue how variation in crystallographic c-axis orientation influences nanomechanical properties of the myostraca and of the non-myostracal hard tissue (Figs. 7, 8 AP6).

4.1. *Is the adductor myostracum microstructure the sole result of a physical growth determinant?*

The evolutionary success of bivalves after the end-Permian mass extinction may not necessarily be based only on variation of shell morphology [98]. The global diversity of bivalves we see today can also be related to their ecological success and remarkable ability to invade new environments and quickly adapt to them [13,99–101].

Within their respective ecological niches, *Glycymeris, Chama* and *Placopecten* are very successful, and their shells are well-adapted to the lifestyles they pursue. Glycymerididae have thick (~5 mm), aragonitic shells. With their transverse visceral musculature, *Glycymeris* are perfectly adapted to burrow into the sediment [102,103]. The two symmetrical adductor muscles comprise smooth and obliquely-striated fibres and are among the strongest within the group of bivalved organisms [103,104]. Organisms belonging to *Chama* are mostly epifaunal and attach their thick (~5 mm) and ornamented shells to a substrate via byssal attachment [60,105]. Studies have shown that chamid shell morphology is adapted to spatial restrictions imposed by the environment [33,106]. Due to their immobility and relatively weak hinge, chamid bivalves developed elongated adductor muscles for rapid valve opening and closure [60,61]. In the Pectinidae, the striated and smooth muscle fibres attach to the shell at a central region and leave a well-visible and large myostracum on the inner surface of the valves [107–109]. Their thin (2–3 mm) calcitic shells and the interplay between ligament and adductor muscle are decisive for their fast swimming rates [15,32,109].

4.1.1. *Similarities in myostracal structure designs*

G. pilosa belongs to the order Arcida, *C. arcana* is a member of Venerida, and *P. magellanicus* belongs to Pectinida. Despite differences in genomics, lifestyle and shell structure, the myostraca of the above-named species show, at first glance, a surprising similarity in myostracal microstructure. It is demonstrated by now that bivalve myostraca are always aragonitic and have a microstructure that varies significantly from the structure of the non-myostracal shells (e.g. [28,34,38,39]). While myostracal crystal growth and microstructure formation appear to be controlled by mainly physical factors, growth of the non-myostracal shell occurs under tighter biological control by the formation of organic membranes confining the morphology of the crystals (e.g. [33,37,42,110]). At myostracal formation, the smooth surface of the non-myostracal shell layer adjacent to the myostracum provides the template for the nucleation of the first-formed myostracal crystals. For *Glycymeris* and *Chama*, these nucleate epitaxially onto the non-myostracal shell layer template [28]. In *P. magellanicus*, the myostracal nucleation is mediated by an organic-rich sheet. The growth of myostracal crystals from the nuclei occurs by a process involving growth competition [28,33,97], i.e. many crystallites are close to each other and compete for space and ions that are needed for them to grow. The likelihood for a crystallite to grow larger is determined by its crystallographic orientation. The growth rate decreases non-linearly with the deviation of the crystal's fastest growth direction (for carbonate materials, the c-axis) from the orientation normal to the nucleation template. With continuing growth, the less favourably oriented crystals become outperformed and overgrown by the more favourably oriented crystals. As the latter grow in length and diameter, a progressively stronger crystallographic preferred orientation develops along the fastest axis of growth (the c-axis in the present case), while the number of crystals in the microstructure decreases with distance away from the nucleation template [28,111,112].

In essence, two distinct processes govern the formation of bivalve myostracal crystals: (i) epitactic nucleation onto a non-myostracal shell layer surface or organic-rich template and (ii) growth of the crystals, driven by the process of growth competition. We find these structural characteristics for the adductor myostraca of the three studied species (Fig. 1).

A further structural similarity we found for the myostraca of the investigated species, irrespective of differences in myostracal crystal size, is the degree and mode of twinning of the myostracal crystals (Fig. 6, AP5). The common aragonitic twin law, corresponding to a misorientation of 63.8° around [001], is a mirror reflection on the {110} plane, which is mostly the composition plane [85]. The misorientation angle diagrams for the myostraca of the three investigated species show a relative misorientation maximum around 64° with relative frequencies of about 15 % (Fig. 6, AP5). This confirms that crystal twinning is prevalent within the adductor myostraca of the investigated bivalves. The red lines superimposed on the band contrast EBSD maps conducted on the myostraca (Fig. 6, AP5) are 64° grain boundaries. The preferred twinning mode for all investigated myostraca is cyclic twinning following the {110} twin law. Since the twinned surfaces are irregular in the present cases and do not strictly seem to follow the regular {110} plane, we consider them to be penetration twins.

4.1.2. *Differences in myostracal structure designs*

Despite the two above-mentioned structural similarities for the

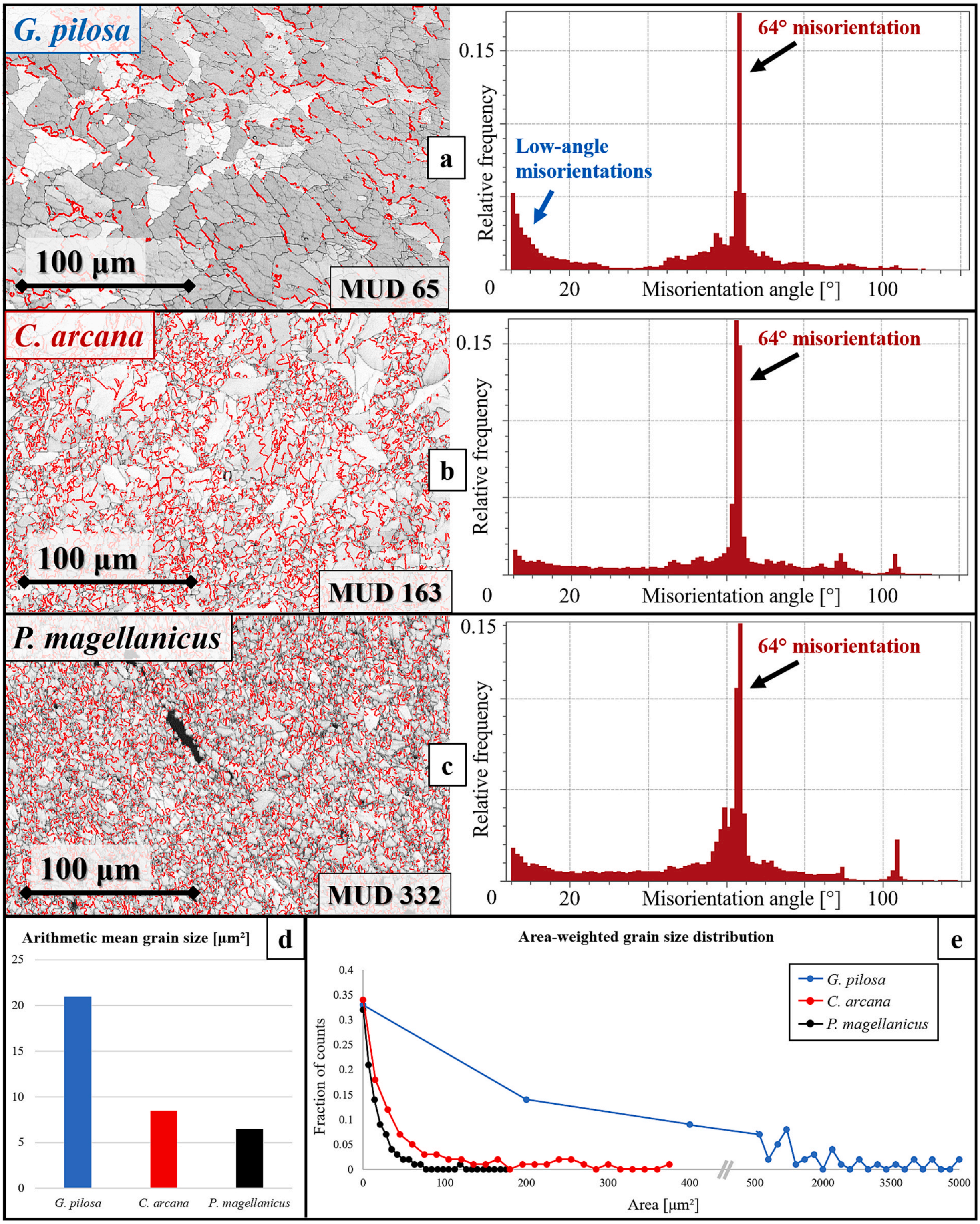

Fig. 6. Misorientation angle distribution and grain size statistics for adductor myostraca sectioned along Cut 2 in *G. pilosa, C. arcana* and *P. magellanicus*. Irrespective of the texture and microstructure, the myostracal prisms of *G. pilosa* (a), *C. arcana* (b) and *P. magellanicus* (c) predominantly follow a grain misorientation angle of about 64°. This angle corresponds to aragonitic twinning on the (110) and $(1\bar{1}0)$ planes, constituting more than 15 % of all analysed grain boundaries (a-c). The average grain size varies considerably between the three microstructures. When cross-sectioned, *G. pilosa* shows the highest average grain size (d), comprising crystals that may exceed a size of 4000 μm^2 (e). *C. arcana* and *P. magellanicus* show similar grain size statistics, however, *C. arcana* crystals appear slightly larger in mean size (d, e).

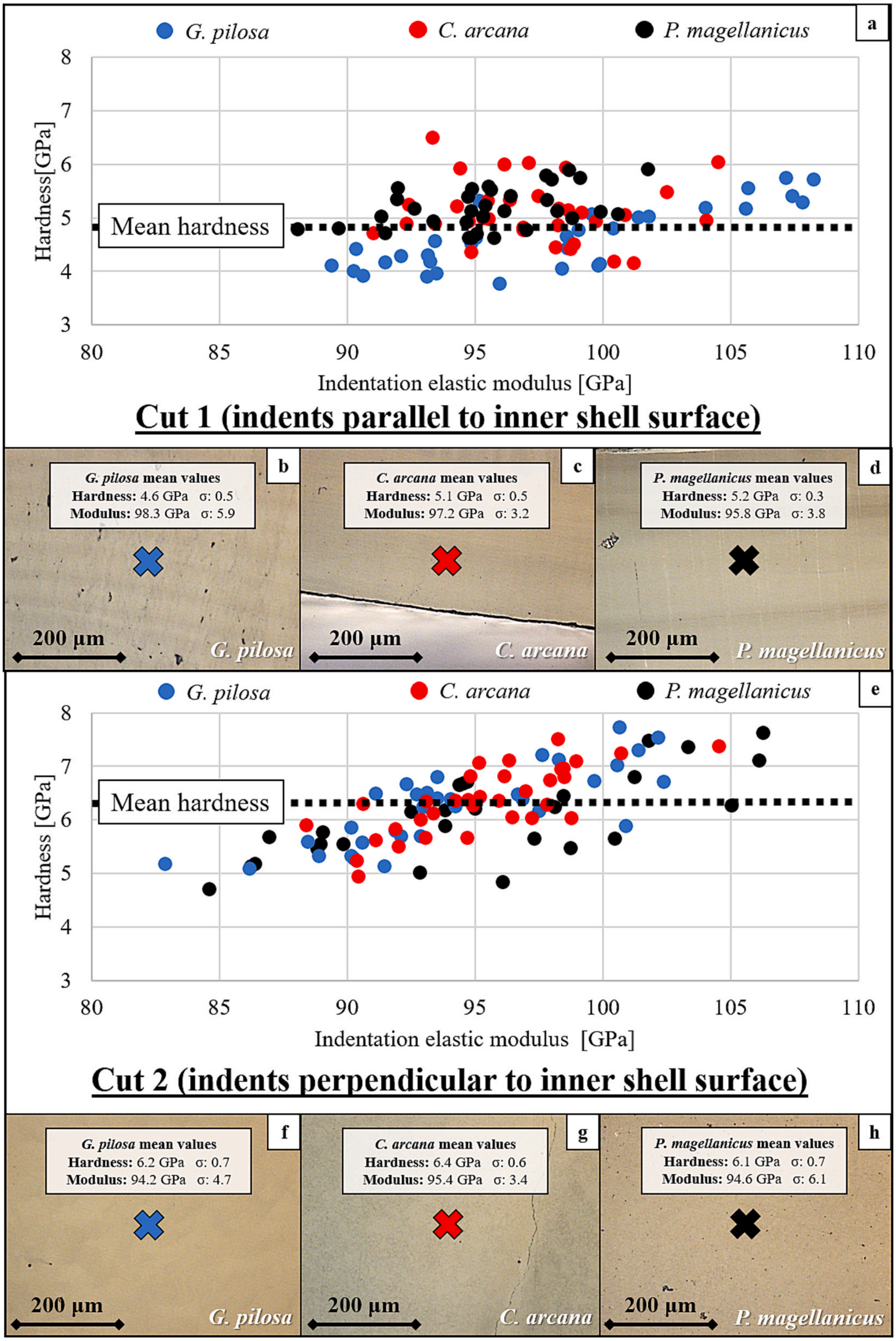

Fig. 7. The hardness and indentation elastic modulus distribution of adductor myostraca in *G. pilosa, C. arcana* and *P. magellanicus* for different indentation directions. The plots show the individual data points of the respective myostraca measured perpendicular (a) or parallel (e) to the orientation of the crystallographic c-axes. The confocal laser microscopy images (b-d) and (f-h) display the corresponding microstructures and give the mean values and standard deviations σ for the hardness and elastic indentation moduli. The measurements show that when indented parallel, rather than perpendicular, to the c-axes, the observed myostracal hardness increases by about 1 GPa. Dotted black lines indicate the mean hardness of the three myostraca indented parallel (a) and perpendicular to the inner shell surface (e). For different indentation directions, the indentation elastic moduli of the respective structures do not show significant differences. The adductor myostraca were indented at similar distances from the changeover with the adjacent shell (Cut 1) or the inner shell surface (Cut 2).

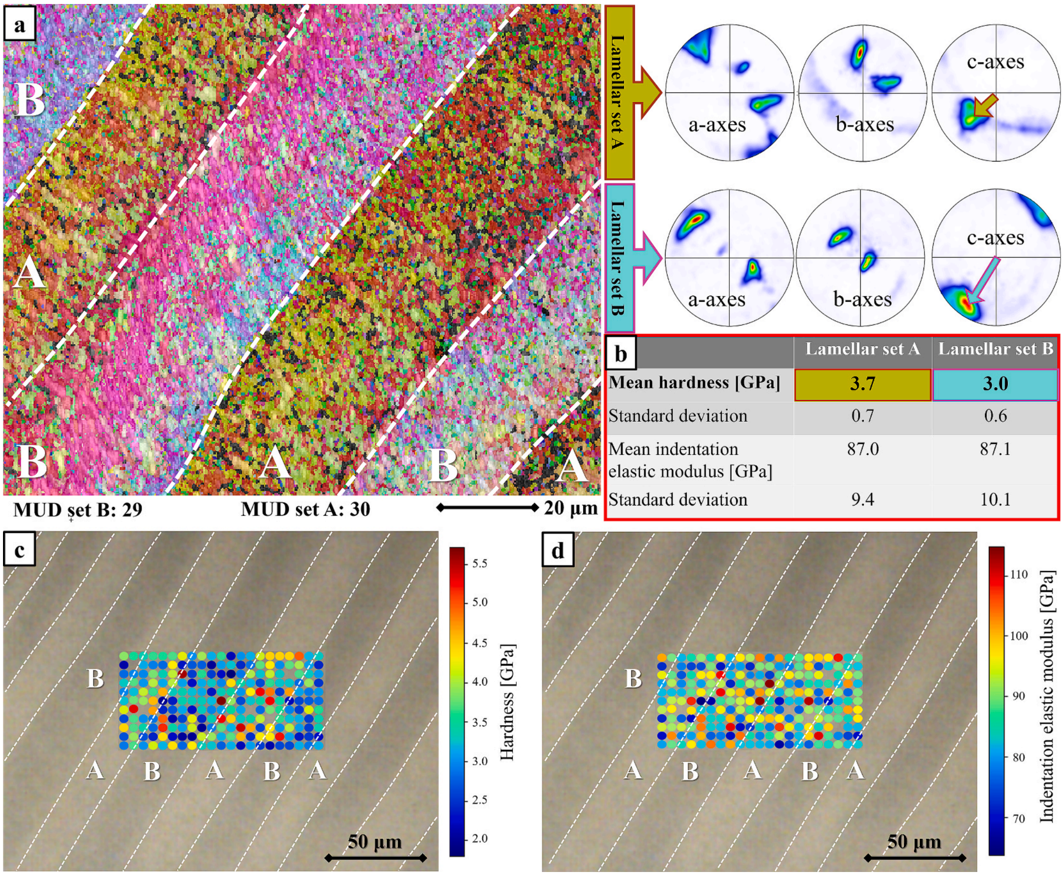

b	Lamellar set A	Lamellar set B
Mean hardness [GPa]	**3.7**	**3.0**
Standard deviation	0.7	0.6
Mean indentation elastic modulus [GPa]	87.0	87.1
Standard deviation	9.4	10.1

Fig. 8. Microstructural and nanomechanical analysis of different sets in the crossed-lamellar layer of *G. pilosa*. A colour-coded EBSD map performed on the shell shows the microstructure and texture of the two sets (a). Both sets are strongly twinned and have a 3D “single-crystal-like” texture, as indicated by the corresponding contoured pole figures (a). Their crystallographic co-orientation is comparable; however, the orientation of the c-axes differs. As indicated by coloured arrows in (a), the crystallographic c-axes of the lamellar set A are slightly tilted towards the indentation direction and the c-axes of set B run perpendicular to the indentation direction. A 100 x 50 μm^2 area spanning three first-order lamellae of the crossed-lamellar layer at a comparable position to the EBSD scan was indented (11 x 21 indents at 5 µm intervals). Table (b) displays the mean hardness and indentation elastic modulus values for sets A and B and gives the respective standard deviations. Set A shows a higher average hardness than set B; no difference can be observed for the elastic indentation moduli (b). The measured hardness (c) and indentation elastic modulus (d) for each indent are superimposed onto a microscopy image, where the first-order lamellar sets A and B are indicated by lines. Points with anomalous indentation curves were excluded from the plot. The positions of the nanoindentation data points and their assignment to set A or B are depicted in Appendix Figure AP7.

myostraca of the investigated bivalves, we find strong structural differences between *G. pilosa*, *C. arcana* and *P. magellanicus* myostraca, namely:

(i) myostracal prism size (EBSD maps in Fig. 2, AP3 and grain size statistics in Fig. 6d, e, AP5),
(ii) crystal co-orientation strength (MUD values in Figs. 1 and 2)
(iii) myostracal texture (pole figures in Fig. 2, AP3).

4.2. *The influence of myostracal prism size and crystal co-orientation strength*

In contrast to *P. magellanicus* and *C. arcana,* we find for *G. pilosa* myostraca an abrupt increase in prism diameter and length close to the changeover from the non-myostracal valve to the myostracum (Fig. 1a). As myostracal crystals increase in size with progressive growth due to a growth competition process, we find crystals with very large cross-sections at the *G. pilosa* myostracal inner surface (Fig. 2a, AP3a, 6d, e). *C. arcana and P. magellanicus* do not show such a sudden increase in prism diameter and size close to the changeover from the non-myostracal valve to the myostracum (Fig. 1b, c). *C. arcana* and particularly *P. magellanicus* myostraca consist of thin and long prisms (up to 5 µm in diameter and 100 µm in length). Accordingly, at the inner myostracal surface, prism cross-sections are rather small (Fig. 2b, c, AP3b, c, Fig. 6d, e).

Contrarily to what was expected from the model of competitive growth, the decrease in prism size from *G. pilosa* via *C. arcana* to *P. magellanicus* along the inner myostracal surfaces (Fig. 2, AP3) is accompanied by an increase in crystal co-orientation strength (see MUD values in Fig. 5a to c). For the *G. pilosa* myostracum, we find an MUD value of 65, while for the *P. magellanicus* myostracum, we find an MUD value of 332 (Fig. 6a, c).

At first glance, this is rather surprising as *G. pilosa* features a 3D “single-crystal-like” texture, and *C. arcana* and *P. magellanicus* show an axial texture. Nevertheless, the difference in crystallographic co-orientation statistics of the three myostraca might be caused by the difference in the orientational variation of the c-axes. As the colours for myostracal crystal orientation in Fig. 1 highlight for *G. pilosa* and, to some extent, for *C. arcana*, myostracal crystal orientations vary significantly between the species. In *G. pilosa*, the misorientation between crystallographic c-axes is inherited from the double maxima of the crossed-lamellar layer. In contrast, for the *P. magellanicus* myostracum, we find a strong crystal coalignment, displayed by the similar colours in the EBSD map (Fig. 2c). A further reason for the difference in crystal co-orientation strength and, hence, MUD value between the myostraca of the investigated species could be that the large prisms of *G. pilosa* are internally more structured. Thus, they comprise many small misorientations (e.g. white stars in Fig. 2a) relative to the degree of internal structuring of the smaller-sized prisms of *C. arcana* and *P. magellanicus*.

4.3. Myostracal and non-myostracal shell texture

The *G. pilosa* adductor myostracum has a 3D "single-crystal-like" texture inherited from the 3D "single-crystal-like" crystal orientation pattern of the adjacent crossed-lamellar shell (compare pole figures in Fig. 1a with pole figures in Fig. 2a, 3a). A crossed-lamellar microstructure consists of a sequence of first-order lamellae, with the latter being composed of crystals forming two orientational sets, set A and set B (e.g. Fig. 8c). For *C. arcana* adductor myostracum and myostracal pillars, the crossed-lamellar crystal orientation pattern of the adjacent shell is, at first, also continued within the myostraca. Within the very first few µm of the myostracum, crystals that belong to the set of the first-order lamellae having their c-axes perpendicular to the shell-myostracum changeover surface, outcompete crystals of the other first-order lamellar set. For *C. arcana*, this results in a gradual shift from the 3D "single crystal-like" texture of the non-myostracal crossed-lamellar shell (see the orientation maxima in the pole figures of Fig. 3b) to an axial texture of the myostracum (see pole figures in Fig. 2b without distinct a- and b-axes).

The shell of *P. magellanicus* is formed of foliated calcite (Fig. 3c, AP2), while the myostracum comprises competitively grown aragonite (Fig. 1b). Thus, the *P. magellanicus* myostracal crystals cannot adopt the texture of the adjacent shell layer. Instead, the changeover from the non-myostracal shell to the myostracum features a thin (around 5 µm thick) organic-rich layer (white star in Fig. 1b, AP2c). This organic-rich layer mediates the interconnection between the *P. magellanicus* calcitic shell and the aragonitic myostracum. Similar sheets separating calcitic and aragonitic shell layers have also been observed for other bivalve species, such as *Chama arcana*, *Crassostrea gigas* or *Pinctada margaritifera* [33,111–113]. The myostracum of *P. magellanicus* has a marked axial texture with aragonite c-axes oriented towards the direction of growth (Fig. 1b) and is highly co-oriented (see pole figures in Fig. 2c, AP3c). The texture of the adjacent non-myostracal shell is axial as well; however, it shows a very low degree of crystal co-orientation strength (see pole figures in Fig. 3c, AP2c). As described above, we find very different crystal co-orientation strengths (MUD values) at the innermost myostracal surface of the three investigated species (Fig. 6a to c). We noted for the investigated species that the longer the texture of the adjacent, non-myostracal shell is continued towards the inner myostracal surface, the lower the myostracal crystal co-orientation strength and the MUD value of the EBSD scan. Of the investigated bivalve species, the *G. pilosa* myostracum adopts, at most, the texture of the adjacent non-myostracal shell; the myostracum has a low crystal co-orientation strength. The *P. magellanicus* myostracum does not adopt the texture of the adjacent non-myostracal shell; its myostracum has the highest crystal co-orientation strength.

4.4. Factors that generate modulation of the competitively grown myostracal structure

4.4.1. The crystallography of shell crystals adjacent to the myostracum and their influence on the myostraca

This and previous studies [28,34,35] highlight that the interface between shell layers, comprising different aragonite microstructures, is not sharp and clear-cut. The transition from one layer to the other is based on the interlinkage of the textures of the adjacent two shell layers.

The three investigated bivalve species have the following shell microstructures adjacent to their myostraca: *G. pilosa* has a crossed-lamellar layer with first-order lamellae running almost perpendicular to the inner shell surface (Fig. AP2a). *C. arcana* also has a crossed-lamellar microstructure adjacent to the adductor myostracum; however, in contrast to the first-order lamellae of *G. pilosa*, the morphology of the first-order lamellae is irregular, and the two sets of first-order lamellae are intertwined (Fig. 3b, AP2b and [33]). The *P. magellanicus* shell adjacent to the adductor myostracum comprises foliated calcite (Fig. AP2c). The colour-coded EBSD maps show that at the changeover from the non-myostracal shell to the myostracum, the very first myostracal crystals of *G. pilosa* and *C. arcana* adopt the texture of the adjacent crossed-lamellar layer (Fig. 1a, d and [28]). This is due to the topotactic nucleation of myostracal nuclei onto the non-myostracal shell surface, as the orientation pattern of shell crystals continues into the adjacent myostracum. The nucleation stage of myostracum formation is biologically determined. Crystallographic characteristics of myostracal crystal nuclei are determined for *G. pilosa* and *C. arcana* by crystallographic characteristics of crystals of the non-myostracal shell and for *P. magellanicus* by an organic substance secreted by the organism.

The *Glycymeris pilosa* case.

Due to the straight morphology of the first-order lamellae in *G. pilosa*, the two sets of first-order lamellae (set A, set B, e.g. Fig. 8c) are well distinguishable. It is also well observable that the crossed-lamellar crystal orientation pattern of the first-order lamellar shell microstructure is continued into and within the *G. pilosa* myostracum (Fig. 1a), up to the inner myostracal surface. The two sets of first-order lamellae have crystallographic c-axes orientations tilted relative to each other (Fig. 3a and [28,114]). As myostracal crystal growth is controlled by growth competition, two different crystal growth speeds develop at the formation of the *G. pilosa* myostracum. Depending on aragonite c-axes inclination relative to the nucleation template, the crystals of one set of first-order lamellae grow faster than the crystals of the other set. The crystals of the fast-growing lamella increase, with ongoing growth, quickly in size (Fig. 1a) and form the very large crystal units that we find at the inner myostracal surface (e.g. Fig. 2a, AP3a), blocking the growth of crystals of the other set of the first-order lamella. Nonetheless, the crystals of the slowly growing set of the first-order lamella are not eliminated entirely, as the two sets of first-order lamellae are, in *G. pilosa*, spatially well distinguished from each other (Fig. 3a). They are not intertwined, as is the case for the shell of *C. arcana* (Fig. 3b).

The *Chama arcana* case.

In *C. arcana* shells as well, the non-myostracal shell layer adjacent to the myostracum has a crossed-lamellar microstructure, and the latter microstructure is continued, at least to some extent, into the adjoining myostracum. However, for the *C. arcana* non-myostracal shell, we find an intricate intertwining of the two sets of the first-order lamellae (Fig. 3b). This causes a tight arrangement of these within the non-myostracal shell as well as at the changeover from the non-myostracal shell to the myostracum. In *C. arcana* shells as well, the two first-order lamellar sets have different c-axis orientations. However, due to the strong intertwining of the two first-order lamellar sets, the set with the crystals having their c-axes oriented precisely perpendicular to the nucleation template fully outcompetes the growth of crystals of the other first-order lamellar set. The result is that crystals of only one crossed-lamellar set remain, and due to their high co-orientation, only one c-axis orientation is kept. This implies that the remaining/kept crystals grow at similar rates and generate the observed *C. arcana* adductor myostracal and myostracal pillar microstructure, formed of similarly-sized, acicular prisms (Fig. 2c, d). An axial texture develops, as only the c-axes are co-oriented, not necessarily the a- and b-axes.

The *Placopecten magellanicus* case.

The shell and myostracum of *P. magellanicus* are a special case. There is a carbonate phase change between the calcite of the non-myostracal shell and the aragonite of the myostracum; thus, structural characteristics are not transmitted from the non-myostracal shell to the adjacent myostracum. Myostracal crystals do not follow a pattern of predetermined orientation inherited from the adjacent valve, as is the case for *G. pilosa* and *C. arcana*. In contrast, *P. magellanicus* myostracal crystals start to grow a few micrometres away from the non-myostracal valve-myostracum interface (Fig. 1b). They are developed as a sequence of thin, long (several tens of micrometres) acicular crystals with high crystal co-orientation and an axial texture. When the microstructure of the *P. magellanicus* adductor myostracum is compared to that of *G. pilosa* and *C. arcana*, for the adductor myostracum of *P. magellanicus*, the typical structure of a material consisting of competitively grown crystals is least observable (Fig. 1a to c, compare the image of adductor myostraca of the investigated species). This is also evident from the crystallographic co-orientation strength that does not increase significantly from the nucleation surface to the inner myostracal surface (Fig. 1b).

4.4.2. Further characteristics influencing adductor myostracum microstructure designs and texture

1 The microstructure at the inner myostracal surface can also be influenced by the thickness of the myostracum layer. The competitive growth mechanism enables the most adequately oriented crystals to outcompete the less adequately oriented crystals and gain in thickness. If the myostracum is thin, the competitive growth mechanism might be interrupted before its final stage, consisting of crystals co-aligned along the fastest-growing axis. Since bivalve muscles change position during shell growth [41], the muscle attachment period defining the myostracal crystal growth differs for each section of the myostracum. In addition, the relative thickness of the adductor myostracum, compared to the thickness of the entire shell, varies considerably for different bivalve species. For most bivalves, the myostracum comprises a substantial part of the shell, constituting up to a third of the shell thickness at muscle attachment sites [111,113,115]. However, some bivalve species show thin (less than 10 μm), stacked myostraca comprising tiny crystals (such as *Anomia ephippium* or *Arctica islandica* [116,117]) or a fine, weakly-developed sheet, barely distinguishable from the non-myostracal valve (such as *Mytilus edulis* or *Tellina planata* [116,118]). Furthermore, it should be noted that valve activity is not just the result of muscle (adductor, pedal) activity but is rather an integrant within the interplay between the resilience and efficiency of the hinge ligament and the resilience and efficiency of the adductor muscles [32]. Accordingly, definite proof of a clear-cut connection between valve thickness and myostracum microstructure cannot be provided easily.

2 Recent studies report that adductor myostraca contain a significant amount of organic substance [111,119]. The latter is not developed as organic envelopes encasing the myostracal prisms [111,119] but is present as collagen-rich fibrils within the myostracal crystals [41,120,121]. We conducted TGA measurements for the microstructures encountered in *G. pilosa* and *P. magellanicus* shells (Fig. AP4b). TGA results show that myostraca are richest in organic substance relative to the foliated and the crossed-lamellar shell layers. Furthermore, we observe differences in organic content between myostracal and non-myostracal shell layers and significant differences in organic content for the myostracum of *G. pilosa* and that of *P. magellanicus* (Fig. AP4). The *P. magellanicus* myostracum consists of an assembly of thin and long prisms (Fig. 1b), while *G. pilosa* forms the largest part of its myostracum of large-sized prismatic crystals (Fig. 1a). Bivalve myostraca are organic–inorganic composites. However, due to the physical growth process of competitive growth that governs myostracal crystal growth, there is no biopolymer extracellular matrix at myostracal shell sections. This contrasts with some non-myostracal shell microstructures that comprise organic matrices filled with minerals. Hence, myostracal prisms are not encased by an organic sheath, and the organic substance is not between but within the prisms. In myostraca, organic matter is present as myofilaments, providing the necessary tight connection for the attaching muscle to the prismatic crystals of the myostracum [41]. *G. pilosa* myostraca are formed of large myostracal prisms; hence, there are few grain interfaces within the *G. pilosa* myostracum. The *G. pilosa* myostracum is most enriched in organic material (Fig. AP4), far more than the *P. magellanicus* myostracum, which comprises many thin prisms and, thus, very many prism interfaces. In addition to the above discussion, we take the latter as a further indication that at myostraca, the organic substance is mainly within the prisms. Nonetheless, it could not be determined whether a specific composition of an organic substance or a specific, proactive arrangement of muscle fibres possibly causes organism-related differences in the structural characteristics of myostraca. For gastropods, it has been reported that differences in structure and thickness of the cross-linked adductor muscle bundles can influence myostracal microstructure [122].

4.5. Nanomechanical properties of myostraca and the non-myostracal shell

The diverse challenges of marine environments for organism survival push biomineralised hard tissues to be as tough and fracture-resistant as possible [48,123–125]. However, in material optimisation, a multi-scale trade-off has to be achieved between adjusting the nanomechanical properties of the hard tissue to meet the requirements needed to generate a lightweight and metabolically cheap structural material. Various factors, such as crystal size, orientation, arrangement, mode of interlinkage, organic substance content, fabric and distribution, influence structural hard tissue's mechanical strength and fracture resistance [28,48,126–128]. Therefore, understanding the effect of crystal orientation and mode of assembly on nanomechanical property results of the structural material is essential, not just for the correct interpretation of the gained results but also to decipher the biomineralisation principles that generate the respective structural biomaterial.

4.5.1. Hardness and indentation elastic modulus

Our study investigated the hardness and indentation elastic modulus of myostracal and non-myostracal valve layers (Figs. 4, 5). We juxtaposed the gained results: (i) for each investigated species between the adductor myostracum and the non-myostracal shell and (ii) for the myostraca of the three investigated species for the two performed cuts (Cut 1, Cut 2) through the shell (Fig. 7).

Irrespective of the indentation direction, the hardness and indentation elastic modulus of the myostraca exceeds the hardness and indentation elastic modulus of the respective non-myostracal shells. Relative to non-biological aragonite, myostracal hardness is increased; however, myostracal indentation elastic modulus is reduced (Table 1). Relative to non-biological aragonite, crossed-lamellar (CL) shell hardness is reduced, while complex crossed-lamellar (CCL) shell hardness is increased (Table 1).

When indented parallel to the inner shell surface (Cut 1), the adductor myostraca of the three investigated species show a mean hardness of about 4.9 GPa (Fig. 7a). Myostracal hardness is lowest (H: 4.6 GPa) for *G. pilosa*, the myostracum that consists of large prisms with a 3D "single-crystal-like" texture inherited from the crossed-lamellar layer (Fig. 1a). In contrast, myostracal hardness is increased (H: 5.1, 5.2 GPa) for the species that form their myostraca of many rather thin prisms with an axial texture (Fig. 1b, c). Table 2 highlights myostracal mean hardness and indentation elastic modulus values for other bivalve species indented parallel to their inner shell surface. The species are sorted in the table by the increasing influence of the competitive growth mechanism on the myostracal microstructure. *Ostrea stentina* (number 1 in Table 2) secretes a myostracum, which is strongly distinct in microstructure from the rest of the calcitic shell, via competitive growth without an aragonitic shell template. In contrast, the microstructure of *Tellina planata* (number 7 in Table 2) myostraca is almost indistinguishable from the microstructure of the rest of the shell layer. Hence, there is little influence of a competitive growth process on myostracal structure formation. The corresponding nanoindentation results indicate that myostraca with a clear-cut competitive growth-derived microstructure character have a higher hardness and elastic indentation modulus relative to those myostraca where the competitive growth-initiated structure is little or almost undeveloped (Table 2). This effect might explain the slightly lower hardness of the *G. pilosa* myostracum relative to the myostracal hardness of *C. arcana* and *P. magellanicus* (described in greater detail in chapter 2.7 of [129]).

Another explanation of the hardness variations includes the size of

Table 2

Nanoindentation results for indentation maps performed on the adductor myostraca of seven bivalve species. The species were sorted by the influence of the competitive growth process on their respective myostracal layers. *Ostrea stentina* (1.) myostraca have a microstructure characteristic for formation through competitive growth. In contrast, *Tellina planata* (7.) myostraca are very similar in structure to the adjacent granular shell, the latter controlled by biological determinants. The mean values for hardness and indentation modulus for myostraca of the seven bivalves indicate a trend to higher hardness and indentation elastic modulus for those myostraca crystallised predominantly under a physical determinant, e.g. *O. stentina*, *Peryglypta puerpera*, *Dosinia scalaris* and *Anomia ephippium*. This contrasts species where myostracum formation is little influenced by the physical determinant of competitive growth. All specimens were sectioned along Cut 1, with the indentation direction parallel to the inner shell surface. Myostracal microstructures and an in-depth analysis of the indentation measurements are reported in chapter 2.7 of [129].

Species	Average myostracal hardness [GPa]	Average myostracal modulus [GPa]
1. *Ostrea stentina*	5.2	99
2. *Periglypta puerpera*	5.1	91
3. *Dosinia scalaris*	4.9	97
4. *Anomia ephippium*	5	94
5. *Mytilus edulis*	4.3	84
6. *Arctica islandica*	3.3	80
7. *Tellina planata*	3.2	71

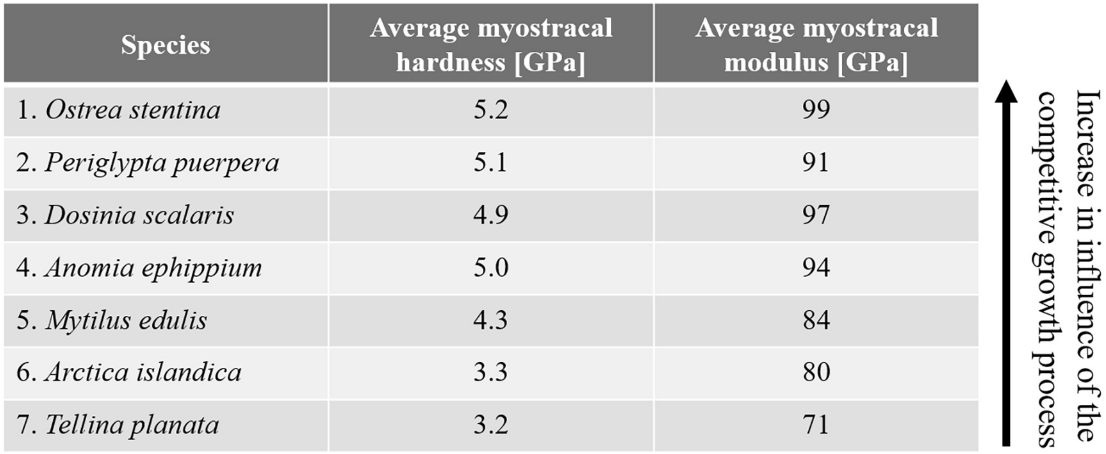

Species	Average myostracal hardness [GPa]	Average myostracal modulus [GPa]
1. *Ostrea stentina*	5.2	99
2. *Periglypta puerpera*	5.1	91
3. *Dosinia scalaris*	4.9	97
4. *Anomia ephippium*	5.0	94
5. *Mytilus edulis*	4.3	84
6. *Arctica islandica*	3.3	80
7. *Tellina planata*	3.2	71

the myostracal prisms: when the shell is sectioned according to Cut 1, the highest hardness is observed for the *P. magellanicus* myostracum, comprising the thinnest and longest prisms of the three investigated myostraca (Fig. 1b). For artificial materials, the Hall-Petch relation [130–133] describes that a decrease in grain size and increase in grain boundary area results in higher yield strength. However, although a similar trend has been reported for biomineralised hard tissues in avian eggshells [134], the Hall-Petch effect is still poorly understood. Accordingly, without additional microstructure-nanomechanical property studies, we cannot unequivocally constrain whether the varying hardness values are a grain size effect. We see a significant difference in myostracal prism thickness between the investigated species (e.g. Fig. 2); however, the difference in hardness is very small (*G. pilosa*: 4.6 GPa; *C. arcana*: 5.1 GPa; *P. magellanicus*: 5.2 GPa) and only observable in Cut 1, when indentation is carried out parallel to the inner shell surface. When indented parallel to the myostracal crystal c-axis (Cut 2), the myostracal hardness for the three investigated bivalve species is similar; the mean hardness is 6.2 GPa (Fig. 7e).

Myostracal indentation elastic modulus is very little affected by the direction of cut through the shell or/and the direction of crystal c-axis orientation (Fig. 7, Table 1). Nonetheless, we observe for the indentation elastic modulus as well a distinct difference between the myostraca and the respective shells (Table 1). The highest indentation modulus we find for non-biological aragonite; the modulus value for the latter is markedly higher than the modulus values of the myostraca and is significantly higher than the modulus values for the respective shells (Table 1).

Previous studies indicate that indentation elastic modulus results gained on biomaterials depend on the organic matrix within the composite hard tissue [135–137], such that an increased organic content in the structural biomaterial induces a decrease in indentation elastic modulus. In our study, we find that compared to geological aragonite, myostracal and non-myostracal indentation elastic moduli are decreased for all investigated species (Table 1). The probable reason for the reduced indentation elastic modulus of the different shell layers, relative to non-biological aragonite, is that organic substance is present in all layers of the investigated shells (Fig. AP4). Nonetheless, crucial for indentation elastic modulus results of biomaterials is not just the amount of organic substance within a microstructure but also its distribution mode. For example, the crossed-lamellar layer of *G. pilosa* has a low organic content (Fig. AP4) but also a distinctly low average indentation elastic modulus (Fig. 4b and Table 1). In contrast, the myostracum of *G. pilosa* has a significantly higher organic substance content (Appendix Figure AP4) and higher indentation elastic modulus values (Table 1). This discrepancy can be explained by the different distributions of the organic substances in the *G. pilosa* crossed-lamellar shell and myostracum. In the crossed-lamellar microstructure, the organic substance forms a thin, matrix-like sheath evenly distributed around every lath. In the myostracum, however, collagen-rich fibrils are found within the prisms and lack from the boundaries of adjacent myostracal prisms. However, it is important to remember that the difference in indentation elastic modulus might also be related to the different microstructures of the adductor myostracum and the respective non-myostracal shell.

We did not measure a significant difference in elastic modulus for the calcite between the inorganic reference and the *P. magellanicus* foliated calcite shell. Of all investigated microstructures, foliated calcite has the least fraction (~1%) of organic matter (Appendix Figure AP4). This could explain the small difference in indentation elastic modulus observed between geological and foliated calcite (Table 1 and Fig. 4c, d). Furthermore, our study shows that for all investigated species and both cuts through the shell, the adductor myostraca have comparable indentation elastic moduli (Fig. 7). Hence, myostracal indentation elastic modulus is neither influenced by crystallographic axes orientation of the constituting crystals, nor by their size or mode of assembly.

4.5.2. *Difference in nanomechanical properties between C. arcana adductor myostraca and myostracal pillars*

Myostracal pillars are, most probably, the result of mantle epithelium attachment and are most common in the Chamacea, where they can occupy a significant fraction of the inner shell layer [25,33,61,138]. They usually arise from the trace of the pallial line and grow towards the inner shell surface, firmly attaching the mantle tissue of the organism to the shell [61]. However, in rare cases, such as in *Cardita variegata*, they can also occupy the marginal section of the outer shell layer [25]. The comparison of *C. arcana* adductor myostracum (Fig. 1c) and myostracal pillar (Fig. 1d) microstructure does not show major structural differences. Both structures comprise long (up to 100 μm) and relatively thin (<5 μm) prismatic crystals and their growth is guided by the competitive growth mechanism. At the changeover from the crossed-lamellar, non-myostracal valve to the myostracal crystal arrangement, the texture of the crossed-lamellar shell is transmitted to the myostracum. The texture of the non-myostracal valve is more or less axial (see pole figures in Fig. 3b, AP2b); it is in-between a 3D “single-crystal-like” and a fully axial texture). The texture of the adjacent myostraca (adductor myostraca, myostracal prisms) is also axial (Fig. 1c, d), and the axial texture is maintained until the inner shell surface. However, nanomechanical property measurements give for the adductor myostracum and the myostracal pillars distinct differences in hardness and indentation elastic modulus (Table 1, Fig. 5). For both cuts through the shell, we find that the myostracal pillars show a lower hardness relative to the adductor myostracum. When indented parallel to the inner shell surface (Cut 1), the hardness between the two layers decreases by 0.6 GPa (Fig. 5a, b) and when indented perpendicular to the inner shell surface (Cut 2), it decreases by 1.0 GPa (Fig. 5c, d). The mean indentation elastic modulus is reduced for myostracal pillars, relative to myostracal elastic modulus, by more than 10 GPa (Fig. 5). Due to the rare occurrence of myostracal pillars in bivalve shells, the attachment mechanism between the mantle epithelium and the shell is poorly understood. However, their low indentation elastic modulus values and microstructure, similar to the myostracum, indicate that the pillars might comprise differences in the distribution of organic matter.

4.5.3. *The anisotropic fracture behaviour of the complex crossed-lamellar layer*

The complex crossed-lamellar layer is a prominent yet poorly understood microstructure that comprises first-order lamellar blocks with more than two dip directions and an axial texture [139]. The blocks consist of strongly twinned, prismatic aragonite crystals with a relatively small grain size of less than 5 μm [28,34]. Although recent studies have shown a “complex crossed-lamellar type” microstructure in the ornamentations of *Chama gryphoides* shells [28,33], in general, the complex crossed-lamellar microstructure forms inner shell layers adjacent to the pallial myostracum. Our nanomechanical property results indicate that the complex crossed-lamellar layer’s response to nanoindentation testing strongly depends on the direction of the cut (Fig. 5, Table 1). When indented parallel to the inner shell surface (Cut 1), the complex crossed-lamellar layer is relatively hard and maintains a relatively low indentation elastic modulus (Fig. 5a, Table 1). These nanomechanical property results are particularly astounding when considering the complex crossed-lamellar layer’s relatively high organic content compared to other shell layers (Appendix Figure AP4 and [140]).

However, when the complex crossed-lamellar shell layer is indented perpendicular to the inner shell surface (Cut 2, Fig. 5b), the recorded load–displacement curves appear irregular and show multiple pop-in events (Figure AP6). These (nano)failures denote rapid tip displacement under contact load, potentially due to shear-induced cracking [141,142]. The localised material failures result in tip sliding and the formation of further penetration/displacement that deteriorates the calculated hardness by including “failure depths”. Thus, we conclude that the low hardness and indentation elastic modulus of the complex crossed-lamellar layer indented parallel to the c-axis orientations

(Fig. 4b, Table 1) are misleading. This "graceful failure" can be amplified when the material is loaded along crystallographic axes directions, promoting faster chipping and cleavage. It is common in quasi-brittle materials and has previously been observed for crossed-lamellar shells, pointing to their anisotropic mechanical behaviour [143–145]. To our knowledge, this is the first study that reports this specific nanomechanical property behaviour for the complex crossed-lamellar microstructure of biological structural materials. Organic material-filled microtubules were observed in the complex crossed-lamellar layer of other molluscs, such as *Neritilia rubida* or *Corbicula fluminea* [146,147]. These microchannels might be responsible for the high overall organic content (Appendix Figure AP4) and the anisotropic pop-in events along indentation perpendicular to the inner shell surface (Appendix Figure AP6).

4.5.4. *The effect of c-axis orientation on hardness and indentation elastic modulus*

Several studies have shown that the orientation of crystals in bivalve shells is often controlled by biological determinants [37,42], even though myostracal crystal growth is guided mainly by a physical determinant. In general, crystallographic c-axes appear perpendicular to shelled organisms' inner and outer shell surfaces [29]. Most likely, the latter is not by chance but is rather a functional property. Thus, testing shell microstructures in a cut parallel to the shell surface is of great interest as it simulates the exposed hard tissue. Previous studies have shown the anisotropic nanomechanical properties of single-crystalline calcite and aragonite [148,149], as well as of biomineralised carbonate microstructures, such as nacre or prismatic calcite [149–151]. The single-crystalline calcite and aragonite were tested with c-axes misoriented 35-40° to the indentation direction to compensate for potential anisotropic effects within the non-biological references. Compared to other directions such as {001}, Deng et al. have recently found that geological calcite shows balanced nanomechanical properties along the {104}-direction [83], comparable to the reference orientations tested in this study (Figure AP7a, b). To our knowledge, this is the first study that investigates the anisotropic behaviour of aragonite crystals in the exceptionally hard bivalve myostraca and the widespread crossed-lamellar shell. Our results demonstrate that adductor myostraca, indented perpendicular to the inner shell surface (Cut 2), have comparable hardness values (Fig. 7e-h). Averaging more than 6 GPa for all three layers, the mean hardness of Cut 2 is significantly higher than the hardness values obtained for Cut 1 (Fig. 7a-d). Interestingly, the indentation elastic modulus values of the three layers are hardly affected by the change in indentation direction (Fig. 7a, e). This indicates that the difference in myostracal hardness is most likely not caused by a difference in organic content for the investigated shells but rather due to the orientation direction of the crystallographic c-axes.

While the indentation elastic modulus is an inherent material property, the measured hardness of biomineralised materials depends on factors such as architectural packing, crystallinity, porosity, organic content, grain size and grain orientation. While many of these factors can vary in biomineralised hard tissues, they are biologically controlled in the crossed-lamellar layers of *Glycymeris* shells. The first-order lamellae of the latter comprise two sets with very similar crystal size, morphology, organic content and porosity (Fig. 3a, 8a in this study and Supplementary Fig. S21 in [34]). However, our (Fig. 3a, 8) and previous studies (e.g., [28,34,114,152]) show that the crystals of the two sets (set A, set B) of first-order lamellae differ notably in orientation. This is well visible by the distinct density distribution maxima of contoured pole figures (see the difference in pole figures in Fig. 8a) displaying the varying c-axis orientations (see arrows within the c-axes pole figures in Fig. 8a).

With the combination of EBSD measurements and indentation testing, we can demonstrate that the obtained hardness values are largely affected by the crystallographic orientation of aragonite c-axes (Fig. 8b). Nanoindentation measurements were performed across a series of first-order-lamellae (Fig. 8c, d, AP7c) and show that the observed hardness changes notably between the two lamellar sets (for hardness distribution see Fig. 8c). In contrast, the indentation elastic modulus values do not show a correlation with one or the other set of first-order lamellae. Despite the relatively high standard deviation caused by the heterogeneity of the crossed-lamellar composite layer, the indentation elastic modulus values are, more or less, similar for the two sets (Fig. 8b, d). The pole figures in Fig. 8a demonstrate that c-axes of crystals of lamellar set A are clustered at an orientation somewhat similar to the indentation direction. In contrast, as the pole figures of Fig. 8a show, the c-axes of crystals that form set B are almost perpendicular to the indentation direction. From the nanomechanical property values in Fig. 8b, we observe that within first-order lamellae of *G. pilosa,* the mean hardness of set A is increased by 0.7 GPa, compared to the mean hardness of set B. Therefore, combining EBSD analysis and nanoindentation testing shows that the hardness is increased for the crystals of set A. In this set, we find a co-alignment of crystal c-axis orientations with the indentation direction relative to crystals of the other set (in this case, set B) of the first-order lamellae. Hence, this study indicates that the characteristics of microstructures, such as presetting crystal c-axis orientation, can influence the hardness of the aragonitic biomaterial. Similar or more sophisticated experimental setups in future experiments may help to precisely demonstrate and understand the relation between crystallographic orientation and nanomechanical properties in biomineralised hard tissues.

The present study compared the results of bivalve shell and myostracal microstructures obtained on different cuts through the hierarchical shells. In general, we found a strong correlation between crystal c-axis orientation and the hardness of the biomaterial. For more or less axial microstructures, the effect of azimuthal variability on nanoindentation measurements can be controlled by investigating the crystallographic texture of the indented surface. However, for microstructures that lack crystallographic co-orientation along a single c-axis direction, as is the case for crossed-lamellar structures, azimuthal variability on nanoindentation causes a significant problem regarding the reproducibility and consistency of hardness results. Accordingly, for nanomechanical property studies of biological hard tissues, it is vital to determine the microstructure and crystallographic texture of the investigated material, not only to understand the hard tissue of one particular specimen or/and species but also to enable comparison of nanomechanical property data between specimens and species. Böhm et al. [153] proposed using conical nanoindentation indenters to analyse biogenic materials and to avoid azimuthal hardness dependence. The latter is not yet widespread for biomineralised materials, and the comparability of results obtained by Berkovich and conical indenters is disputed [154–157].

5. Conclusions

Bivalved organisms occupy a wide ecological space and can adapt to many lifestyles and environments [12–14,95,100,158]. This is enabled by developing various microstructure designs, occluding biopolymers into the hard tissue, and generating hierarchical structures. The latter characteristics are the keys to material optimisation, environment adaptation and survival. The valves of bivalve organisms are secreted not only to protect their soft tissue but also to burrow into the sediment, attach to a substrate via cementation, and perform locomotion for swimming. The muscles that control valve activity and the muscle attachment sites to the valves are integral to the organism's success in living a particular lifestyle and surviving in a specific environment. In the present contribution, we discuss the interlinkage of the non-myostracal and myostracal valve microstructure, texture and nanomechanical properties for bivalves using valve activity to burrow, swim, or be epifaunal and sessile. Combining EBSD measurements with nanoindentation testing on valves sectioned perpendicular and parallel to the inner shell surface, we decipher structural approaches utilised by the investigated organisms to optimise their shell material for leading the above-mentioned lifestyles. We deduce from our results the following conclusions:

1. *G. pilosa* and *C. arcana* influence the microstructure and texture of their myostraca by controlling the structural properties of the non-myostracal shell adjacent to the myostracum, the template used for myostracal crystal nucleation. Even if for different bivalve species, the shell layer adjacent to the myostracum is similar in microstructure (e.g., crossed-lamellar, as is the case for *G. pilosa* and *C. arcana*), minor differences in the pattern of crystal orientation of the non-myostracal shell affect the adjacent myostracal microstructure strongly, since, at similar carbonate phase, the crystallographic texture of the shell is transmitted to the myostracum.For interdigitated or/and thin first-order lamellae (*C. arcana*), the crystals of the transmitted set of first-order lamellae, with their c-axes being perpendicular to the nucleation template and facing towards the growth direction, can quickly outcompete their neighbours. As the remaining co-oriented crystals can no longer gain lateral space, the corresponding myostraca are formed of thin, acicular crystals with an axial texture. For morphologically well-regulated or/and thick first-order lamellae (*G. pilosa*), the progressive elimination of crystals with divergent c-axis orientations to the nucleation template is prolonged. This results in a myostracal microstructure consisting of thick prisms and leading to the 3D “single-crystal-like” texture, extending from the non-myostracal valve to the inner myostracal surface.
2. *P. magellanicus*, *G. pilosa* and *C. arcana* myostraca are aragonitic. If the valve layer adjacent to the myostracum is calcitic, as for *P. magellanicus*, the orientation pattern of the non-myostracal calcite crystals is not transmitted to the adjacent aragonitic myostracum. If the shell layer adjoining the myostracum is aragonitic, as is the case for *G. pilosa* and *C. arcana*, the first-formed myostracal crystals assume the orientation of crystals of the adjacent aragonitic shell.
3. Myostracal microstructure, texture, prism morphology and size do not affect the mode or frequency of twinning of myostracal aragonite. The twinning of myostracal aragonite is extensive, and the extent of twin formation is similar for all investigated species. The twins are cyclic by (110) and $(1\bar{1}0)$ twin laws and generate a multitude of twin boundaries. These are of main structural importance, as it is shown for manufactured materials that the incorporation of twin boundaries increases the mechanical properties of the material.
4. Nanomechanical results demonstrate that, compared to non-myostracal layers and inorganic aragonite, myostracal aragonite has an increased hardness and indentation elastic modulus. Myostracal prism size and morphology do not influence the nanomechanical properties of the myostracum.
5. Even if the microstructure and prism size is similar for *C. arcana* adductor myostraca and myostracal pillars, nanomechanical properties differ for the latter structures. The decrease in hardness and indentation elastic modulus of myostracal pillars, relative to the nanomechanical properties of the adductor myostracum, might be due to a different distribution of organic substance within the pillars, in comparison to the distribution of biopolymers within the adductor myostracum.
6. The indentation elastic moduli for the species and shell layers investigated in this study are not only influenced by the sheer amount of organic substance in the different microstructures but, in particular, by the mode of biopolymer distribution within the layer and microstructure.
7. The hardness values obtained for the non-myostracal shell and the myostraca differ significantly, depending on the angle between the indentation direction and crystal c-axis orientation. Layers indented parallel to the crystallographic c-axis orientation show the highest hardness, while crystals indented perpendicular to the c-axis orientation have a reduced hardness. For the indentation elastic modulus, the indentation direction is also influenced by crystal c-axis orientation. However, it is significantly less pronounced than what is observed for the hardness.
8. Furthermore, the anisotropic effect of indentation on hardness is demonstrated in this study for the two sets of a first-order lamella in the crossed-lamellar shell microstructure of *G. pilosa*. In the latter, the average hardness of set A of a first-order lamella (c-axes oriented almost parallel to the indentation direction) is significantly higher than the hardness of set B of the same first-order lamella (c-axes oriented perpendicular to the indentation direction).
9. Nanomechanical properties of the complex crossed-lamellar shell layer vary drastically with indentation direction. When indented parallel to the inner shell surface, the layer appears quite brittle and shows an average hardness similar to myostracal pillars. When indented perpendicular to the inner shell surface, the complex crossed-lamellar layer is subject to many pop-in events, indicating the formation of microcracks and/or lattice dislocations.

In essence, even though the crystal growth mechanism of *G. pilosa, C. arcana* and *P. magellanicus* myostraca is similar, we find, for the investigated bivalve species, significant differences in myostracal structural designs as well as in the crystallographic and structural characteristics of myostracal crystals. Our study demonstrates that, in contrast to previous reports [34,43,97], the structure of bivalve myostraca is not conservative. Differences in myostracal structure are rooted in the fact that myostracal formation combines two processes: crystal nucleation and crystal growth. Myostracal crystal nucleation is influenced by the structural characteristics of the adjacent, non-myostracal shell. In contrast, the formation of the myostracal microstructure is mainly subjected to the physical process of growth competition, rather than being controlled by the formation of organic membranes prior to crystallisation. It is predetermined by structural features transmitted from the biologically controlled non-myostracal shell to the myostraca. In addition, the combination and interplay of different types of fibres forming a muscle affect myostracal structure, as observed in the well-distinguishable muscle fibre imprints of the smooth and striated muscles of *P. magellanicus*.

We conducted an extended study on bivalve myostracal structure, microstructure, and texture (this study and [28,33,116–118,159]) and found that the crystallographic characteristics for bivalve myostraca, determined with EBSD, are not family-specific. For example, the myostracal structure and crystallographic characteristics we found for *P. magellanicus* (Pectinidae) were also detected for the myostracum of *Ostrea stentina* (Ostreidae). Likewise, the myostracal structure and crystallographic characteristics of *G. pilosa* (Glycymerididae) are also observable in the shells of *Dosinia scalaris* (Veneridae) and *Anadara polii* (Arcidae). Myostracal structural features of *C. arcana* (Chamidae) are also present in the shells of *Acanthocardia tuberculata* (Cardiidae), *Periglypta puerpera* (Veneridae) and *Lampsilis cardium* (Unionidae). Keeping in mind the highly specialised shell structures that bivalves developed to maximise their chances of survival (such as different microstructural motifs [29,160–162] or ornamentations [61,163,164]), it is remarkable that the myostracal structure, microstructure, texture and formation mechanism is comparable across bivalve families. While myostracal microstructure and texture are also influenced by other requirements, e.g. environmental characteristics, their design is largely predetermined by biologically controlled and proactive templates, such as adjacent aragonitic shell layers or organic-rich sheets.

CRediT authorship contribution statement

S. Hoerl: Writing – review & editing, Writing – original draft, Visualization, Methodology, Investigation, Data curation, Conceptualization. **C. Micheletti:** Writing – review & editing, Visualization, Software, Investigation, Data curation. **S. Amini:** Validation, Supervision,

Software, Investigation, Conceptualization. **E. Griesshaber:** Writing – review & editing, Validation, Supervision, Methodology, Investigation, Data curation, Conceptualization. **K.-U. Hess:** . **A.G. Checa:** Writing – review & editing, Validation, Formal analysis. **M. Peharda:** Writing – review & editing, Validation, Resources. **W.W. Schmahl:** Writing – review & editing, Supervision, Project administration, Funding acquisition, Formal analysis.

Declaration of competing interest

The authors declare that they have no known competing financial interests or personal relationships that could have appeared to influence the work reported in this paper.

Acknowledgements

We thank Prof. N. Lagos Suárez, Centro de Investigación e Innovación para el Cambio Climático – CIICC, Universidad Santo Tomas, Santiago, Chile, Prof. E.M. Harper, Department of Earth Sciences, University of Cambridge, Downing Street, Cambridge CB2 3EQ, U.K. and Prof. C. Salas and Prof. S. Gofas, Departamento de Biología Animal, Facultad de Ciencias, Universidad de Málaga, Málaga, Spain for the samples.

W. W. S., E. G., and S.H. were funded by the German Research Council Programmes GR 9/1234, SCHM 930/11-2. A. G. C. was funded by the project PID2020116660GB-I00 of the Spanish Ministerio de Ciencia e Innovación (MCIN/AEI/10.13039/501100011033/). A. G. C. acknowledges the Research Group RNM363 (CEICE, JA) and the Unidad Científica de Excelencia UCE-PP2016-05 (University of Granada).

Appendix A. Supplementary data

Supplementary data to this article can be found online at https://doi.org/10.1016/j.matdes.2025.113845.

Data availability

Data will be made available on request.

References

[1] R. Bieler, P.M. Mikkelsen, G. Giribet, Bivalvia—A discussion of known unknowns*, Am. Malacol. Bull. 31 (2013) 123–133, https://doi.org/10.4003/006.031.0105.
[2] P.M. Mikkelsen, Speciation in modern marine bivalves (Mollusca: Bivalvia): Insights from the published record*,, Am. Malacol. Bull. 29 (2011) 217–245, https://doi.org/10.4003/006.029.0212.
[3] R.N. Hughes, A functional biology of marine gastropods, Johns Hopkins Univ. Pr, Baltimore, Md, 1986.
[4] S.R. Palumbi, Genetic divergence, reproductive isolation, and marine speciation, Annu. Rev. Ecol. Syst. 25 (1994) 547–572, https://doi.org/10.1146/annurev.es.25.110194.002555.
[5] B.P. Kinlan, S.D. Gaines, Propagule dispersal in marine and terrestrial environments: a community perspective, Ecology 84 (2003) 2007–2020, https://doi.org/10.1890/01-0622.
[6] R.D. Norris, P.M. Hull, The temporal dimension of marine speciation, Evol. Ecol. 26 (2012) 393–415, https://doi.org/10.1007/s10682-011-9488-4.
[7] N. Bierne, F. Bonhomme, P. David, Habitat preference and the marine-speciation paradox, Proc. R. Soc. Lond. B Biol. Sci. 270 (2003) 1399–1406, https://doi.org/10.1098/rspb.2003.2404.
[8] G.M. Kamenev, V.V. Mordukhovich, I.L. Alalykina, A.V. Chernyshev, A. S. Maiorova, Macrofauna and nematode abundance in the Aayssal and hadal zones of interconnected deep-sea ecosystems in the Kuril Basin (Sea of Okhotsk) and the Kuril-Kamchatka Trench (Pacific Ocean), Front. Mar. Sci. 9 (2022) 812464, https://doi.org/10.3389/fmars.2022.812464.
[9] E.M. Krylova, G.M. Kamenev, I.P. Vladychenskaya, N.B. Petrov, Vesicomyinae (Bivalvia: Vesicomyidae) of the Kuril–Kamchatka Trench and adjacent abyssal regions, Deep Sea Res, Part II Top. Stud. Oceanogr. 111 (2015) 198–209, https://doi.org/10.1016/j.dsr2.2014.10.004.
[10] A. Iglikowska, J. Przytarska, E. Humphreys-Williams, J. Najorka, M. Chełchowski, A. Sowa, H. Hop, M. Włodarska-Kowalczuk, P. Kukliński, Shell mineralogy and chemistry – Arctic bivalves in a global context, Mar. Pollut. Bull. 189 (2023) 114759, https://doi.org/10.1016/j.marpolbul.2023.114759.
[11] J. Norkko, A. Norkko, S.F. Thrush, V.J. Cummings, Detecting growth under environmental extremes: Spatial and temporal patterns in nucleic acid ratios in two Antarctic bivalves, J. Exp. Mar. Biol. Ecol. 326 (2005) 144–156, https://doi.org/10.1016/j.jembe.2005.05.014.
[12] N. Sharma, S. Mondal, S. Ganguly, A. Giri, Substrate- and life habit-induced morphological convergence and divergence in Recent marine bivalve communities, Biol. J. Linn. Soc. 140 (2023) 120–129, https://doi.org/10.1093/biolinnean/blad031.
[13] S.M. Stanley, Functional morphology and evolution of byssally attached bivalve mollusks, J. Paleontol. 165–212 (1972).
[14] E.R. Trueman, A.R. Brand, P. Davis, The dynamics of burrowing of some common littoral bivalves, J. Exp. Biol. 44 (1966) 469–492, https://doi.org/10.1242/jeb.44.3.469.
[15] H.E. Guderley, I. Tremblay, Swimming in scallops, in: Dev. Aquac. Fish. Sci., Elsevier, 2016: pp. 535–566.
[16] S.M. Stanley, Relation of shell form to life habits of the Bivalvia (Mollusca), The Geological Society of America, Boulder, Colo, 1970.
[17] K.S. Collins, S.M. Edie, D. Jablonski, Convergence and contingency in the evolution of a specialized mode of life: multiple origins and high disparity of rock-boring bivalves, Proc. R. Soc. B Biol. Sci. 290 (2023) 20221907, https://doi.org/10.1098/rspb.2022.1907.
[18] J. Kobak, Factors influencing the attachment strength of *Dreissena polymorpha* (Bivalvia), Biofouling 22 (2006) 141–150, https://doi.org/10.1080/08927010600691895.
[19] R.M.C. Eagar, Shape and function of the shell: A comparison of some living and fossil bivalve molluscs, Biol. Rev. 53 (1978) 169–210, https://doi.org/10.1111/j.1469-185X.1978.tb01436.x.
[20] F.R.S.D. Silva, A.L.D.O. Borges, E.E. Toldo Jr., C. Fick, E. Puhl, V.C.B. Oliveira, F. E.G.D. Cruz, Threshold of motion and orientation of bivalve shells under current flow, Braz. J. Geol. 53 (2023) e20220080, https://doi.org/10.1590/2317-4889202320220080.
[21] J.A. Audino, J.M. Serb, J.E.A.R. Marian, Hard to get, easy to lose: Evolution of mantle photoreceptor organs in bivalves (Bivalvia, Pteriomorphia), Evol. 74 (2020) 2105–2120, https://doi.org/10.1111/evo.14050.
[22] B. Morton, The evolution of eyes in the Bivalvia, Oceanogr. Mar. Biol. Annu. Rev. 39 (2001) 165–205.
[23] S.M. De Paula, M. Silveira, Studies on molluscan shells: Contributions from microscopic and analytical methods, Micron 40 (2009) 669–690, https://doi.org/10.1016/j.micron.2009.05.006.
[24] N. Watabe, Shell repair, in, The Mollusca, Elsevier (1983) 289–316, https://doi.org/10.1016/B978-0-12-751404-8.50015-3.
[25] J. Taylor, W. Kennedy, A. Hall, The shell structure and mineralogy of the Bivalvia. II. Lucinacea-Clavagellacea, conclusions, Bull. Br. Mus. Nat. Hist. Zool. 22 (1973) 255–294. Doi: 10.5962/p.314199.
[26] N. Spann, E.M. Harper, D.C. Aldridge, The unusual mineral vaterite in shells of the freshwater bivalve Corbicula fluminea from the UK, Naturwissenschaften 97 (2010) 743–751, https://doi.org/10.1007/s00114-010-0692-9.
[27] L. Qiao, Q.L. Feng, Y. Liu, A novel bio-vaterite in freshwater pearls with high thermal stability and low dissolubility, Mater. Lett. 62 (2008) 1793–1796, https://doi.org/10.1016/j.matlet.2007.10.023.
[28] S. Hoerl, T. Le Moine, N.J. Peter, S. Amini, E. Griesshaber, J. Wang, E.M. Harper, C. Salas, A.G. Checa, R. Schwaiger, W.W. Schmahl, Crystal organisation and material properties of Chama and Glycymeris myostraca and shells, Materialia 36 (2024) 102149, https://doi.org/10.1016/j.mtla.2024.102149.
[29] A.G. Checa, E. Griesshaber, C. Salas, L. Angiolini, W.W. Schmahl, Mollusc and brachiopod carbonate biomineralization, in: P. Fratzl, L.M. Liz-Marzán, N.A. Kotov (Eds.), Biominer. Bioinspired Compos., 2024.
[30] A. Iglikowska, J. Bełdowski, M. Chełchowski, M. Chierici, M. Kędra, J. Przytarska, A. Sowa, P. Kukliński, Chemical composition of two mineralogically contrasting Arctic bivalves' shells and their relationships to environmental variables, Mar. Pollut. Bull. 114 (2017) 903–916, https://doi.org/10.1016/j.marpolbul.2016.10.071.
[31] J.A. Crame, Intrinsic and extrinsic controls on the diversification of the Bivalvia, in: S.J. Culver, P.F. Rawson (Eds.), Biot. Response Glob. Change, 1st ed., Cambridge University Press, 2000: pp. 135–148. Doi: 10.1017/CBO9780511535505.011.
[32] I. Tremblay, M. Samson-Dô, H.E. Guderley, When behavior and mechanics meet: Scallop swimming capacities and their hinge ligament, J. Shellfish Res. 34 (2015) 203–212, https://doi.org/10.2983/035.034.0201.
[33] S. Hoerl, E. Griesshaber, A.G. Checa, W.W. Schmahl, The biological crystals in chamid bivalve shells: Diversity in morphology and crystal arrangement pattern, Crystals 14 (2024) 649, https://doi.org/10.3390/cryst14070649.
[34] G. Crippa, E. Griesshaber, A.G. Checa, E.M. Harper, M.S. Roda, W.W. Schmahl, Orientation patterns of aragonitic crossed-lamellar, fibrous prismatic and myostracal microstructures of modern *Glycymeris* shells, J. Struct. Biol. 212 (2020), https://doi.org/10.1016/j.jsb.2020.107653.
[35] G. Crippa, E. Griesshaber, A.G. Checa, E.M. Harper, M.S. Roda, W.W. Schmahl, Sem, ebsd,, laser confocal microscopy and FE-SEM data from modern *Glycymeris* shell layers, Data Brief 33 (2020) 106547, https://doi.org/10.1016/j.dib.2020.106547.
[36] W.J. Kennedy, J.D. Taylor, A. Hall, Environmental and biological controls on bivalve shell mineralogy, Biol. Rev. 44 (1969) 499–530, https://doi.org/10.1111/j.1469-185X.1969.tb00610.x.
[37] J.-P. Cuif, M. Burghammer, V. Chamard, Y. Dauphin, P. Godard, G. Moullac, G. Nehrke, A. Perez-Huerta, Evidence of a biological control over origin, growth

and end of the calcite prisms in the shells of *Pinctada margaritifera* (Pelecypod, Pterioidea), Minerals 4 (2014) 815–834, https://doi.org/10.3390/min4040815.

[38] A.G. Checa, Physical and biological determinants of the fabrication of molluscan shell microstructures, Front. Mar. Sci. 5 (2018) 353.

[39] L. Addadi, D. Joester, F. Nudelman, S. Weiner, Mollusk shell formation: A source of new concepts for understanding biomineralization processes, Chem. – Eur. J. 12 (2006) 980–987, https://doi.org/10.1002/chem.200500980.

[40] F. Marin, N. Le Roy, B. Marie, The formation and mineralization of mollusk shell, Front Biosci 4 (2012) 1099–1125.

[41] J.D. Castro-Claros, A. Checa, C. Lucena, J.R. Pearson, C. Salas, Shell-adductor muscle attachment and Ca^{2+} transport in the bivalves *Ostrea stentina* and *Anomia ephippium*, Acta Biomater. 120 (2021) 249–262, https://doi.org/10.1016/j.actbio.2020.09.053.

[42] S. Weiner, L. Addadi, Design strategies in mineralized biological materials, J. Mater. Chem. 7 (1997) 689–702.

[43] H.A. Lowenstam, S. Weiner, On biomineralization, Oxford Univ. Press, New York, NY, 1989.

[44] M. Suzuki, H. Nagasawa, Mollusk shell structures and their formation mechanism, Can. J. Zool. 91 (2013) 349–366, https://doi.org/10.1139/cjz-2012-0333.

[45] M.S. Clark, L.S. Peck, J. Arivalagan, T. Backeljau, S. Berland, J.C.R. Cardoso, C. Caurcel, G. Chapelle, M. De Noia, S. Dupont, et al., Deciphering mollusc shell production: the roles of genetic mechanisms through to ecology, aquaculture and biomimetics, Biol. Rev. 95 (2020) 1812–1837, https://doi.org/10.1111/brv.12640.

[46] M. Suzuki, S. Nakayama, H. Nagasawa, T. Kogure, Initial formation of calcite crystals in the thin prismatic layer with the periostracum of *Pinctada fucata*, Micron 45 (2013) 136–139, https://doi.org/10.1016/j.micron.2012.10.010.

[47] M. Lopes-Lima, A. Rocha, F. Gonçalves, J. Andrade, J. Machado, Microstructural characterization of inner shell layers in the freshwater bivalve *Anodonta cygnea*, J. Shellfish Res. 29 (2010) 969–973, https://doi.org/10.2983/035.029.0431.

[48] N.J. Peter, E. Griesshaber, C. Reisecker, S. Hild, M.V.G. Oliveira, W.W. Schmahl, A.S. Schneider, Biocrystal assembly patterns, biopolymer distribution and material property relationships in *Mytilus galloprovincialis*, Bivalvia, and *Haliotis glabra*, Gastropoda, Shells, Materialia 28 (2023) 101749, https://doi.org/10.1016/j.mtla.2023.101749.

[49] M. Peharda, B.A. Black, A. Purroy, H. Mihanović, The bivalve *Glycymeris pilosa* as a multidecadal environmental archive for the Adriatic and Mediterranean Seas, Mar. Environ. Res. 119 (2016) 79–87.

[50] M. Peharda, E.O. Walliser, K. Markulin, A. Purroy, H. Uvanović, I. Janeković, I. Župan, I. Vilibić, B.R. Schöne, *Glycymeris pilosa* (Bivalvia) – A high-potential geochemical archive of the environmental variability in the Adriatic Sea, Mar. Environ. Res. 150 (2019) 104759, https://doi.org/10.1016/j.marenvres.2019.104759.

[51] M. Peharda, M. Crnčević, I. Bušelić, C.A. Richardson, D. Ezgeta-Balić, Growth and longevity of *Glycymeris nummaria* (Linnaeus, 1758) from the eastern Adriatic, Croatia, J. Shellfish Res. 31 (2012) 947–950.

[52] D.J. Reynolds, P.G. Butler, S.M. Williams, J.D. Scourse, C.A. Richardson, A. D. Wanamaker, W.E.N. Austin, A.G. Cage, M.D.J. Sayer, A multiproxy reconstruction of Hebridean (NW Scotland) spring sea surface temperatures between AD 1805 and 2010, Palaeogeogr. Palaeoclimatol. Palaeoecol. 386 (2013) 275–285, https://doi.org/10.1016/j.palaeo.2013.05.029.

[53] A.M. Featherstone, P.G. Butler, M. Peharda, L. Chauvaud, J. Thébault, Influence of riverine input on the growth of *Glycymeris glycymeris* in the Bay of Brest, North-West France, PLOS ONE 12 (2017) e0189782, https://doi.org/10.1371/journal.pone.0189782.

[54] W.M. Brocas, D.J. Reynolds, P.G. Butler, C.A. Richardson, J.D. Scourse, I. D. Ridgway, K. Ramsay, The dog cockle, *Glycymeris glycymeris* (L.), a new annually-resolved sclerochronological archive for the Irish Sea, Palaeogeogr. Palaeoclimatol. Palaeoecol. 373 (2013) 133–140, https://doi.org/10.1016/j.palaeo.2012.03.030.

[55] R.D.K. Thomas, Shell form and the ecological range of living and extinct Arcoida, Paleobiology 4 (1978) 181–194.

[56] M. Legac, M. Hrs-Brenko, A review of bivalve species in the eastern Adriatic Sea. III. Pteriomorpha (Glycymerididae), Nat. Croat. Period. Musei Hist. Nat. Croat. 8 (1999) 9–25.

[57] F.R. Bernard, Living Chamidae of the Eastern Pacific (Bivalve: Heterdonta), Contrib. Sci. 278 (1976) 1–43, https://doi.org/10.5962/p.214207.

[58] D. Nicol, Nomenclatural review of genera and subgenera of Chamidae, J. Wash. Acad. Sci. 42 (1952) 154–156.

[59] J. Allen, On the biology and functional morphology of *Chama gryphoides* Linne (Bivalvia; Chamidae), Vie Milieu 26 (1976) 243–260.

[60] M. Yonge, Form, habit and evolution in the Chamidae (Bivalvia) with reference to conditions in the rudists (Hippuritacea), Philos. Trans. R. Soc. Lond. B. Biol. Sci. 252 (1967) 49–105.

[61] J.W. Kennedy, N.J. Morris, J.D. Taylor, The shell structure, mineralogy and relationships of the Chamacea (Bivalvia), Paleontology 13 (1970) 379–413.

[62] J.L. Manuel, M.J. Dadswell, Swimming of juvenile sea scallops, *Placopecten magellanicus* (Gmelin): A minimum size for effective swimming? J. Exp. Mar. Biol. Ecol. 174 (1993) 137–175, https://doi.org/10.1016/0022-0981(93)90015-G.

[63] A. Labrecque, H. Guderley, Size, muscle metabolic capacities and escape response behaviour in the giant scallop, Aquat. Biol. 13 (2011) 51–64, https://doi.org/10.3354/ab00342.

[64] J.D. Carey, K.D.E. Stokesbury, An assessment of juvenile and adult sea scallop, *Placopecten magellanicus* , distribution in the Northwest Atlantic using high-resolution still imagery, J. Shellfish Res. 30 (2011) 569–582, https://doi.org/10.2983/035.030.0301.

[65] K.D.E. Stokesbury, C.E. O'Keefe, B.P. Harris, Fisheries sea scallop, *Placopecten magellanicus*, in: Dev. Aquac. Fish. Sci., Elsevier, 2016: pp. 719–736. Doi: 10.1016/B978-0-444-62710-0.00016-X.

[66] C.M. Pearce, J.L. Manuel, S.M. Gallager, D.A. Manning, R.K. O'Dor, E. Bourget, Depth and timing of settlement of veligers from different populations of giant scallop, *Placopecten magellanicus* (Gmelin), in thermally stratified mesocosms, J. Exp. Mar. Biol. Ecol. 312 (2004) 187–214, https://doi.org/10.1016/j.jembe.2004.06.011.

[67] R.H. Baird, On the swimming behaviour of scallops (*Pecten maximus* L.), J. Molluscan Stud. 33 (1958) 67–71, https://doi.org/10.1093/oxfordjournals.mollus.a064802.

[68] K.D.E. Stokesbury, J.H. Himmelman, Experimental examination of movement of the giant scallop, *Placopecten magellanicus*, Mar. Biol. 124 (1996) 651–660.

[69] J.F. Caddy, Underwater Observations on Scallop (*Placopecten magellanicus*) Behaviour and Drag Efficiency, J. Fish. Res. Board Can. 25 (1968) 2123–2141, https://doi.org/10.1139/f68-189.

[70] J.F. Caddy, Progressive loss of byssus attachment with size in the sea scallop, *Placopecten magellanicus* (Gmelin), J. Exp. Mar. Biol. Ecol. 9 (1972) 179–190, https://doi.org/10.1016/0022-0981(72)90047-0.

[71] M.J. Dadswell, D. Weihs, Size-related hydrodynamic characteristics of the giant scallop, *Placopecten magellanicus* (Bivalvia: Pectinidae), Can. J. Zool. 68 (1990) 778–785, https://doi.org/10.1139/z90-112.

[72] E.R. Trueman, Locomotion in molluscs, in, The Mollusca, Elsevier (1983) 155–198, https://doi.org/10.1016/B978-0-12-751404-8.50012-8.

[73] J.-Y. Cheng, I.G. Davison, M.E. Demont, Dynamics and energetics of scallop locomotion, J. Exp. Biol. 199 (1996) 1931–1946, https://doi.org/10.1242/jeb.199.9.1931.

[74] G.M. Carter, J.L. Henshall, R.J. Wakeman, Knoop hardness and fracture anisotropy of calcite, J. Mater. Sci. Lett. 12 (1993) 407–410, https://doi.org/10.1007/BF00609168.

[75] Y.H. Han, H. Li, T.Y. Wong, R.C. Bradt, Knoop microhardness anisotropy of single-crystal aragonite, J. Am. Ceram. Soc. 74 (1991) 3129–3132, https://doi.org/10.1111/j.1151-2916.1991.tb04311.x.

[76] R.E. Newnham, Properties of materials: anisotropy, symmetry, structure, Oxford University Press (2004), https://doi.org/10.1093/oso/9780198520757.001.0001.

[77] C.A. Brookes, J.B. O'Neill, B.A.W. Redfern, Anisotropy in the hardness of single crystals, Proc. R. Soc. Lond. Math. Phys. Sci. 322 (1971) 73–88, https://doi.org/10.1098/rspa.1971.0055.

[78] D. Banabic, H.-J. Bunge, K. Pöhlandt, A.E. Tekkaya, Formability of metallic materials: plastic anisotropy, formability testing, forming limits, Springer, Berlin Heidelberg, Berlin, Heidelberg, 2000.

[79] K.J. Bowman, R. Moon, E. Drewry, S. Wan, P. Tortorici, M.A. Dayananda, Anisotropic properties in textured ceramics, Mater. Sci. Forum 273–275 (1998) 587–594, https://doi.org/10.4028/www.scientific.net/MSF.273-275.587.

[80] B. Hutchinson, Critical Assessment 16: Anisotropy in metals, Mater. Sci. Technol. 31 (2015) 1393–1401, https://doi.org/10.1179/1743284715Y.0000000118.

[81] G.R. Anstis, P. Chantikul, B.R. Lawn, D.B. Marshall, A critical evaluation of indentation techniques for measuring fracture toughness: I, Direct crack measurements, J. Am. Ceram. Soc. 64 (1981) 533–538, https://doi.org/10.1111/j.1151-2916.1981.tb10320.x.

[82] W.C. Oliver, G.M. Pharr, An improved technique for determining hardness and elastic modulus using load and displacement sensing indentation experiments, J. Mater. Res. 7 (1992) 1564–1583.

[83] Z. Deng, L. Chen, L. Li, Comparative nanoindentation study of biogenic and geological calcite, J. Mech. Behav. Biomed. Mater. 137 (2023) 105538, https://doi.org/10.1016/j.jmbbm.2022.105538.

[84] A.J. Schwartz, M. Kumar, B.L. Adams, D.P. Field, eds., Electron backscatter diffraction in materials science, Springer US, Boston, MA, 2009. Doi: 10.1007/978-0-387-88136-2.

[85] Th. Hahn, H. Klapper, Twinning of crystals, in: Int. Tables Crystallogr., John Wiley & Sons, Ltd, 2013: pp. 413–483. Doi: 10.1107/97809553602060000917.

[86] E. Griesshaber, W.W. Schmahl, H.S. Ubhi, J. Huber, F. Nindiyasari, B. Maier, A. Ziegler, Homoepitaxial meso- and microscale crystal co-orientation and organic matrix network structure in Mytilus edulis nacre and calcite, Acta Biomater. 9 (2013) 9492–9502, https://doi.org/10.1016/j.actbio.2013.07.020.

[87] T. Kogure, M. Suzuki, H. Kim, H. Mukai, A.G. Checa, T. Sasaki, H. Nagasawa, Twin density of aragonite in molluscan shells characterized using X-ray diffraction and transmission electron microscopy, J. Cryst. Growth 397 (2014) 39–46, https://doi.org/10.1016/j.jcrysgro.2014.03.029.

[88] P. Chantler, Biochemical and structural aspects of molluscan muscle, in, The Mollusca, Elsevier (1983) 77–154.

[89] J. Squire, The structures of striated and smooth muscles related to their function, in: Muscle Contract. Cell Motil. Mol. Cell. Asp., Springer, 1992: pp. 87–131.

[90] W.W. Dowd, A.G. Jimenez, High-shore mussels, *Mytilus californianus*, have larger muscle fibers with lower aerobic capacities than low-shore conspecifics, Mar. Biol. 166 (2019) 22, https://doi.org/10.1007/s00227-019-3471-y.

[91] J. Hanson, J. Lowy, Structure and function of the contractile apparatus in the muscles of invertebrate animals, in: G.H. Bourne (Ed.), Struct, Academic Press, New York, Funct. Muscle, 1960, pp. 265–335.

[92] N. Odintsova, V. Dyachuk, A. Karpenko, Development of the muscle system and contractile activity in the mussel *Mytilus trossulus* (Mollusca, Bivalvia), Russ. J. Dev. Biol. 38 (2007) 190–196.

[93] D. Funabara, S. Kanoh, M.J. Siegman, T.M. Butler, D.J. Hartshorne, S. Watabe, Twitchin as a regulator of catch contraction in molluscan smooth muscle,

J. Muscle Res. Cell Motil. 26 (2006) 455–460, https://doi.org/10.1007/s10974-005-9029-2.
[94] J.C. Rüegg, Smooth muscle tone, Physiol. Rev. 51 (1971) 201–248.
[95] B.M. Millman, Mechanisms of contraction in molluscan muscle, Am. Zool. 7 (1967) 583–591.
[96] S. Reindl, G. Haszprunar, Fine structure of caeca and mantle of arcoid and limopsoid bivalves (Mollusca: Pteriomorpha), Veliger 39 (1996) 101–116.
[97] W. Dong, J. Huang, C. Liu, H. Wang, G. Zhang, L. Xie, R. Zhang, Characterization of the myostracum layers in molluscs reveals a conservative shell structure, Front. Mar. Sci. 9 (2022) 862929, https://doi.org/10.3389/fmars.2022.862929.
[98] M.L. Fraiser, D.J. Bottjer, When bivalves took over the world, Paleobiology 33 (2007) 397–413, https://doi.org/10.1666/05072.1.
[99] A.E. Bogan, Global diversity of freshwater mussels (Mollusca, Bivalvia) in freshwater, Hydrobiologia 595 (2008) 139–147, https://doi.org/10.1007/s10750-007-9011-7.
[100] A. McLachlan, E. Jaramillo, O. Defeo, J. Dugan, A. De Ruyck, P. Coetzee, Adaptations of bivalves to different beach types, J. Exp. Mar. Biol. Ecol. 187 (1995) 147–160, https://doi.org/10.1016/0022-0981(94)00176-E.
[101] G.J. Vermeij, The mesozoic marine revolution: Evidence from snails, predators and grazers, Paleobiology 3 (1977) 245–258.
[102] A.D. Ansell, E.R. Trueman, Observations on burrowing in *Glycymeris glycymeris* (L.) (Bivalvia, Arcacea), J. Exp. Mar. Biol. Ecol. 1 (1967) 65–75, https://doi.org/10.1016/0022-0981(67)90007-X.
[103] R.D.K. Thomas, Functional morphology, ecology, and evolutionary conservatism in the Glycymerididae (Bivalvia), Palaeontology 18 (1975) 217–254.
[104] F. Plateau, Recherches sur la force absolue des muscles des Invertébrés: 2. Force Absolue Des Muscles Adducteurs Des Mollusques Lamellibranches, Bull. Acad. R. Sci. Belg. 6 (1883) 226–259.
[105] F. Crocetta, P. Russo, The alien spreading of *Chama pacifica* Broderip, 1835 (Mollusca: Bivalvia: Chamidae) in the Mediterranean Sea, Turk. J. Zool. (2013), https://doi.org/10.3906/zoo-1110-28.
[106] G. Pastorino, The genus *Chama* Linné (Bivalvia) in the marine Quaternary of northern Patagonia, Argentina, J. Paleontol. 65 (1991) 756–760, https://doi.org/10.1017/S0022336000037756.
[107] S.M. Cragg, The adductor and retractor muscles of the veliger of *Pecten maximus* (L.)(Bivalvia), J. Molluscan Stud. 51 (1985) 276–283, https://doi.org/10.1093/oxfordjournals.mollus.a065917.
[108] Ø. Andersen, J.S. Torgersen, H.H. Pagander, T. Magnesen, I.A. Johnston, Gene expression analyses of essential catch factors in the smooth and striated adductor muscles of larval, juvenile and adult great scallop (*Pecten maximus*), J. Muscle Res. Cell Motil. 30 (2009) 233–242, https://doi.org/10.1007/s10974-009-9192-y.
[109] R.L. Marsh, J.M. Olson, S.K. Guzik, Mechanical performance of scallop adductor muscle during swimming, Nature 357 (1992) 411–413, https://doi.org/10.1038/357411a0.
[110] A.G. Checa, F.J. Esteban-Delgado, A.B. Rodríguez-Navarro, Crystallographic structure of the foliated calcite of bivalves, J. Struct. Biol. 157 (2007) 393–402, https://doi.org/10.1016/j.jsb.2006.09.005.
[111] S.W. Lee, C.S. Choi, The correlation between organic matrices and biominerals (myostracal prism and folia) of the adult oyster shell, *Crassostrea* test *gigas*, Micron 38 (2007) 58–64, https://doi.org/10.1016/j.micron.2006.03.018.
[112] J.-P. Cuif, C. Lo, Y. Dauphin, Evidence of a scheduled end for prism growth in the shell of *Pinctada margaritifera*: closure of the calcite biomineralization area by a specific organic membrane, Minerals 14 (2023) 20, https://doi.org/10.3390/min14010020.
[113] S.-W. Lee, Y.-N. Jang, J.-C. Kim, Characteristics of the Aragonitic Layer in Adult Oyster Shells, *Crassostrea gigas* : Structural Study of Myostracum including the Adductor Muscle Scar, Evid. Based Complement. Alternat. Med. 2011 (2011) 1–10, https://doi.org/10.1155/2011/742963.
[114] Í. Almagro, P. Drzymała, A.B. Rodríguez-Navarro, C.I. Sainz-Díaz, M.G. Willinger, J. Bonarski, A.G. Checa, Crystallography and textural aspects of crossed lamellar layers in Arcidae (Bivalvia, Mollusca) shells, Key Eng. Mater. 672 (2016) 60–70, https://doi.org/10.4028/www.scientific.net/KEM.672.60.
[115] K. Sato, T. Sasaki, Shell microstructure of Protobranchia (Mollusca: Bivalvia): Diversity, new microstructures and systematic implications, Malacologia 59 (2015) 45–103, https://doi.org/10.4002/040.059.0106.
[116] F.H. Hampa, Crystal assembly patterns of biocarbonate materials, Master's Thesis, Ludwig-Maximilians-Universität (2023).
[117] T. le Moine, Characterization of the microstructure and the texture of calcium carbonate crystals in bivalve shells, Master's Thesis, Ludwig-Maximilians-Universität (2022).
[118] S. Hoerl, Dependency between crystal organization and material properties in bivalve shells, Master's Thesis, Ludwig-Maximilians-Universität (2022).
[119] Z. Liao, L. Bao, M. Fan, P. Gao, X. Wang, C. Qin, X. Li, In-depth proteomic analysis of nacre, prism, and myostracum of *Mytilus* shell, J. Proteomics 122 (2015) 26–40, https://doi.org/10.1016/j.jprot.2015.03.027.
[120] P.S. Galtsoff, The American oyster, *Crassostrea virginica* Gmelin, US Government Printing Office, 1964.
[121] C. Zhao, L. Ren, Q. Liu, T. Liu, Morphological and confocal laser scanning microscopic investigations of the adductor muscle-shell interface in scallop: Morphological and CLSM investigations, Microsc. Res. Tech. 78 (2015) 761–770, https://doi.org/10.1002/jemt.22537.
[122] A.S. Tompa, N. Watabe, Ultrastructural investigation of the mechanism of muscle attachment to the gastropod shell, J. Morphol. 149 (1976) 339–351, https://doi.org/10.1002/jmor.1051490304.
[123] R.O. Ritchie, Toughening materials: enhancing resistance to fracture, Philos. Trans. R. Soc. Math. Phys. Eng. Sci. 379 (2021) 20200437, https://doi.org/10.1098/rsta.2020.0437.
[124] R.O. Ritchie, The conflicts between strength and toughness, Nat. Mater. 10 (2011) 817–822, https://doi.org/10.1038/nmat3115.
[125] C. Bignardi, M. Petraroli, N.M. Pugno, Nanoindentations on conch shells of gastropoda and bivalvia molluscs reveal anisotropic evolution against external attacks, J. Nanosci. Nanotechnol. 10 (2010) 6453–6460, https://doi.org/10.1166/jnn.2010.2626.
[126] J. Taylor, M. Layman, The mechanical properties of bivalve (Mollusca) shell structures, Palaeontology 15 (1972) 73–87.
[127] O.P. Troncoso, F.G. Torres, J. Arroyo, K.N. Gonzales, M. Fernández-García, D. López, Mechanical properties of calcite- and aragonite-based structures by nanoindentation tests, Bioinspired Biomim. Nanobiomaterials 9 (2020) 112–121, https://doi.org/10.1680/jbibn.19.00069.
[128] A.J. Lew, C.A. Stifler, A. Tits, C.A. Schmidt, A. Scholl, A. Cantamessa, L. Müller, Y. Delaunois, P. Compère, D. Ruffoni, M.J. Buehler, P.U.P.A. Gilbert, A molecular-scale understanding of misorientation toughening in corals and seashells, Adv. Mater. 35 (2023) 2300373, https://doi.org/10.1002/adma.202300373.
[129] S. Hoerl, Microstructure, texture and material property determinants of carbonate biominerals, Ph.D. Thesis, Ludwig-Maximilians-Universität (2025).
[130] W.D. Callister Jr, D.G. Rethwisch, Materials science and engineering: an introduction, John wiley & sons, S.I., 2020.
[131] J.T. Wang, D.L. Yin, J.Q. Liu, J. Tao, Y.L. Su, X. Zhao, Effect of grain size on mechanical property of Mg–3Al–1Zn alloy, Scr. Mater. 59 (2008) 63–66, https://doi.org/10.1016/j.scriptamat.2008.02.029.
[132] C. Luo, X. Yang, J. Li, Tensile and compressive mechanical properties of nanocrystalline calcite with grain size effect, J. Mech. 39 (2023) 442–450, https://doi.org/10.1093/jom/ufad033.
[133] N. Hansen, Hall–Petch relation and boundary strengthening, Scr. Mater. 51 (2004) 801–806.
[134] D. Athanasiadou, W. Jiang, D. Goldbaum, A. Saleem, K. Basu, M.S. Pacella, C. F. Böhm, R.R. Chromik, M.T. Hincke, A.B. Rodríguez-Navarro, H. Vali, S.E. Wolf, J.J. Gray, K.H. Bui, M.D. McKee, Nanostructure, osteopontin, and mechanical properties of calcitic avian eggshell, Sci. Adv. 4 (2018) eaar3219, https://doi.org/10.1126/sciadv.aar3219.
[135] M. Dietiker, Nanoindentation of gold nanostructures and nacre-like nanocomposites: size effects and limits of strength, ETH Zurich (2011), https://doi.org/10.3929/ETHZ-A-006707714.
[136] M. O'Toole-Howes, R. Ingleby, M. Mertesdorf, J. Dean, W. Li, M.A. Carpenter, E. M. Harper, Deconvolution of the elastic properties of bivalve shell nanocomposites from direct measurement and finite element analysis, J. Mater. Res. 34 (2019) 2869–2880, https://doi.org/10.1557/jmr.2019.159.
[137] F. Song, A.K. Soh, Y.L. Bai, Structural and mechanical properties of the organic matrix layers of nacre, Biomater. 24 (2003) 3623–3631, https://doi.org/10.1016/S0142-9612(03)00215-1.
[138] L. Doguzhaeva, H. Mutvei, Functional interpretation of inner shell layers in Triassic ceratid ammonites, Lethaia 19 (1986) 195–209.
[139] D. Chateigner, C. Hedegaard, H.-R. Wenk, Mollusc shell microstructures and crystallographic textures, J. Struct. Geol. 22 (2000) 1723–1735, https://doi.org/10.1016/S0191-8141(00)00088-2.
[140] M. De Noia, L. Telesca, D.L.J. Vendrami, H.K. Gokalp, G. Charrier, E.M. Harper, J. I. Hoffman, Population genetic structure is unrelated to shell shape, thickness and organic content in European populations of the soft-shell clam *Mya arenaria*, Genes 11 (2020) 298, https://doi.org/10.3390/genes11030298.
[141] S. Amini, M. Tadayon, S. Idapalapati, A. Miserez, The role of quasi-plasticity in the extreme contact damage tolerance of the stomatopod dactyl club, Nat. Mater. 14 (2015) 943–950, https://doi.org/10.1038/nmat4309.
[142] S.S. Kasyap, K. Senetakis, Application of nanoindentation in the characterization of a porous material with a clastic texture, Mater. 14 (2021) 4579, https://doi.org/10.3390/ma14164579.
[143] J.D. Currey, A.J. Kohn, Fracture in the crossed-lamellar structure of *Conus* shells, J. Mater. Sci. 11 (1976) 1615–1623, https://doi.org/10.1007/BF00737517.
[144] M.A. Meyers, P.-Y. Chen, A.-Y.-M. Lin, Y. Seki, Biological materials: Structure and mechanical properties, Prog. Mater. Sci. 53 (2008) 1–206, https://doi.org/10.1016/j.pmatsci.2007.05.002.
[145] I. Ichim, Q. Li, W. Li, M.V. Swain, J. Kieser, Modelling of fracture behaviour in biomaterials, Biomater. 28 (2007) 1317–1326, https://doi.org/10.1016/j.biomaterials.2006.10.035.
[146] Y. Kano, T. Kase, Systematics of the *Neritilia rubida* complex (Gastropoda: Neritiliidae): Three amphidromous species with overlapping distributions in the Indo-Pacific, J. Molluscan Stud. 69 (2003) 273–284, https://doi.org/10.1093/mollus/69.3.273.
[147] R. Araujo, M.A. Ramos, J. Bedoya, Microtubules in the shell of the invasive bivalve *Corbicula fluminea* (Muller, 1774)(Bivalvia: Heterodonta), J. Molluscan Stud. 60 (1994) 406–413, https://doi.org/10.1093/mollus/60.4.406.
[148] A. Berman, J. Hanson, L. Leiserowitz, T.F. Koetzle, S. Weiner, L. Addadi, Biological control of crystal texture: A widespread strategy for adapting crystal properties to function, Science 259 (1993) 776–779, https://doi.org/10.1126/science.259.5096.776.
[149] L. Pasquini, A. Molinari, P. Fantazzini, Y. Dauphen, J.-P. Cuif, O. Levy, Z. Dubinsky, E. Caroselli, F. Prada, S. Goffredo, M. Di Giosia, M. Reggi, G. Falini, Isotropic microscale mechanical properties of coral skeletons, J. R. Soc. Interface 12 (2015) 20150168, https://doi.org/10.1098/rsif.2015.0168.
[150] F. Barthelat, H. Espinosa, An experimental investigation of deformation and fracture of nacre–mother of pearl, Exp. Mech. 47 (2007) 311–324.

[151] M. Strąg, Ł. Maj, M. Bieda, P. Petrzak, A. Jarzębska, J. Gluch, E. Topal, K. Kutukova, A. Clausner, W. Heyn, K. Berent, K. Nalepka, E. Zschech, A.G. Checa, K. Sztwiertnia, Anisotropy of mechanical properties of *Pinctada margaritifera* mollusk shell, Nanomaterials 10 (2020) 634, https://doi.org/10.3390/nano10040634.

[152] I. Almagro, P. Drzymała, K. Berent, C.I. Sainz-Díaz, M.G. Willinger, J. Bonarski, A. G. Checa, New crystallographic relationships in biogenic aragonite: The crossed-lamellar microstructures of mollusks, Cryst. Growth Des. 16 (2016) 2083–2093, https://doi.org/10.1021/acs.cgd.5b01775.

[153] C.F. Böhm, B. Demmert, J. Harris, T. Fey, F. Marin, S.E. Wolf, Structural commonalities and deviations in the hierarchical organization of crossed-lamellar shells: A case study on the shell of the bivalve *Glycymeris glycymeris*, J. Mater. Res. 31 (2016) 536–546, https://doi.org/10.1557/jmr.2016.46.

[154] N.A. Sakharova, J.V. Fernandes, J.M. Antunes, M.C. Oliveira, Comparison between Berkovich, Vickers and conical indentation tests: A three-dimensional numerical simulation study, Int. J. Solids Struct. 46 (2009) 1095–1104, https://doi.org/10.1016/j.ijsolstr.2008.10.032.

[155] L. Min, C. Wei-min, L. Nai-gang, W. Ling-Dong, A numerical study of indentation using indenters of different geometry, J. Mater. Res. 19 (2004) 73–78, https://doi.org/10.1557/jmr.2004.19.1.73.

[156] S. Swaddiwudhipong, J. Hua, K.K. Tho, Z.S. Liu, Equivalency of Berkovich and conical load-indentation curves, Model. Simul. Mater. Sci. Eng. 14 (2006) 71–82, https://doi.org/10.1088/0965-0393/14/1/006.

[157] S.W. Moore, M.T. Manzari, Y.-L. Shen, Nanoindentation in elastoplastic materials: insights from numerical simulations, Int. J. Smart Nano Mater. 1 (2010) 95–114, https://doi.org/10.1080/19475411003589889.

[158] S.M. Stanley, Relation of shell form to life habits of the Bivalvia (Mollusca), in: Geol. Soc. Am. Mem., Geological Society of America, 1970: pp. 1–282. Doi: 10.1130/MEM125-p1.

[159] P.A. Rathi, Modes of carbonate crystal organization at muscle attachment sites of bivalve shells, Master's Thesis, Ludwig-Maximilians-Universität (2023).

[160] J. Taylor, W. Kennedy, A. Hall, The shell structure and mineralogy of the Bivalvia, Introduction. Nuculacea - Trigonacea, Bull. Br. Mus. Nat. Hist. Zool. Supplement 3 (1969).

[161] J. Carter, P. Harries, N. Malchus, A. Sartori, L. Anderson, R. Bieler, A. Bogan, E. Eugene Coan, J. Cope, S. Cragg, Illustrated glossary of the Bivalvia: treatise online, part N, Revised, Chapter 31, vol 1. Kansas University Paleontological Institute, Lawrence, (2012).

[162] O.B. Boggild, The shell structure of the mollusks, Det K, Dan. Vidensk. Selsk. Skr. Naturvidenskabelig Og Math. Afd. Raekke 9 (2) (1930) 231–326.

[163] T. Ubukata, Theoretical morphology of bivalve shell sculptures, Paleobiology 31 (2005) 643–655.

[164] F. Ye, M.A. Bitner, G.R. Shi, Variation of shell ornamentation with latitude and water depth—A case study using living brachiopods, Ecol. Evol. 13 (2023) e10006, https://doi.org/10.1002/ece3.10006.